Supporting Information

Silicene, Siloxene, or Silicane? Revealing the Structure and Optical Properties of Silicon Nanosheets Derived from Calcium Disilicide

Bradley J. Ryan,[†] Michael P. Hanrahan,[‡,§] Yujie Wang,[†,⊥] Utkarsh Ramesh,[†,⊥] Charles K. A. Nyamekye,[‡,§] Rainie D. Nelson,[†] Zhaoyu Liu,[§,∥] Chuankun Huang,[§,∥] Bevan Whitehead,[§] Jigang Wang,[§,∥] Luke T. Roling,[†] Emily A. Smith,[‡,§] Aaron J. Rossini,[‡,§] and Matthew G. Panthani*[,†]

[†]Department of Chemical and Biological Engineering, Iowa State University, Ames, Iowa 50011, United States of America
[‡]Department of Chemistry, Iowa State University, Ames, Iowa 50011, United States of America
[§]U.S. Department of Energy, Ames Laboratory, Ames, Iowa 50011, United States of America
[∥]Department of Physics and Astronomy, Iowa State University, Ames, Iowa 50011, United States of America
[⊥]These authors contributed equally to this work.

Table of Contents:

Table of Figures:

List of Tables:

Experimental NMR Procedures:

DEPTH,[1] back to back (BABA) double quantum single quantum (DQ–SQ),[2–4] proton detected (dipolar) CP-HETCOR,[5–7] proton detected (scalar) CP-refocused INEPT,[8–11] rotor synchronized MAS CP-CPMG[12] and CP-INADEQUATE[13] were performed with previously reported pulse sequences. The rotor synchronized MAS INEPT-CPMG was performed by combining the INEPT coherence transfer block with CPMG detection. For all experiments, the radiofrequency (rf) fields used for $\pi/2$ pulses were 100 kHz and 62–77 kHz for ^{1}H and ^{29}Si, respectively. The rf fields used for the CP match conditions were experimentally optimized on the samples and were between 33-41 kHz and 53-71 kHz for ^{29}Si and ^{1}H, respectively. The ^{1}H CP match rf was ramped linearly from 85% to 100% of the rf to broaden the CP match condition. For the INEPT experiments, the eDUMBO$_{1-22}$[14] homonuclear decoupling scheme was applied during the scalar evolution periods. The eDUMBO$_{1-22}$ pulses were 32 μs in length with a ^{1}H rf field of 100 kHz. For the τ curve, the duration of the τ' period was set to a 1.44 ms (45 eDUMBO$_{1-22}$ pulses) and the τ period was incremented in steps of 5 eDUMBO$_{1-22}$ pulses. The τ' curve was obtained in the same manner as the τ curve. For the ^{29}Si INEPT 1D and the ^{1}H-^{29}Si CP refocused INEPT 2D, the τ period was sent to 1.44 ms (maximum signal) and the τ' period was set to 0.8-2.21 ms (as indicated on the individual spectra). For the 2D CP refocused-INADEQUATE experiment, the mixing time ($\tau_{1/4J}$) was experimentally optimized and set to 6 ms, which corresponds to an approximate ^{29}Si-^{29}Si J coupling of ~40 Hz. All ^{29}Si detected experiments (with the exception of the ^{29}Si direct excitation) were acquired with CPMG detection and the individual echoes were co-added using the software NUTs 2017 with homebuilt scripts. This includes the 2D CP refocused-INADEQUATE. Peak fitting of the ^{29}Si direct excitation SSNMR spectrum was performed using the solid lineshape analysis (SOLA) program provided in the Bruker Topspin version 3.5 software. For the number of scans, recycle delays, experiment time, and CPMG parameters, see Table S1.

Table S1. SSNMR experimental parameters used to obtain the spectra shown in the manuscript.

Experiment	Recycle Delay (s)	MAS Rate (kHz)	Number of Scans[a]	CPMG Parameters[b]	Experiment Time (min.)
^{1}H DEPTH	1.95	25	32	-	1
1H-1H DQ-SQ BABA	0.75	25	16x320	-	71
1D ^{29}Si-^{1}H CPMAS CPMG (0.5 ms CP contact time)	1.95	25	1024	30x17	34
1D ^{29}Si-^{1}H CPMAS CPMG (3 ms CP contact time)	1.95	25	1024	30x17	34
1D ^{29}Si-^{1}H CPMAS CPMG (6 ms CP contact time)	1.95	25	1024	30x17	34
2D ^{1}H-^{29}Si CPHETCOR (1 ms CP Back contact time)[c]	1.95	25	64x128	-	322
2D ^{1}H-^{29}Si CPHETCOR (6 ms CP Back contact time)[c]	1.95	25	64x128	-	324
1D ^{29}Si-^{1}H INEPT CPMG (τ' = 0.8 ms)[d]	1.95	22.222	1024	30x15	35
1D ^{29}Si-^{1}H INEPT CPMG (τ' = 1.44 ms)[d]	1.95	22.222	1024	30x15	35
1D ^{29}Si-^{1}H INEPT CPMG (τ' = 2.21 ms)[d]	1.95	22.222	1024	30x15	35
2D ^{1}H-^{29}Si CP-refocused INEPT HETCOR (τ' = 1.44 ms)	1.95	22	64x128	-	333
2D ^{1}H-^{29}Si CP-refocused INEPT HETCOR (τ' = 2.21 ms)	1.95	22	64x128	-	333
2D ^{29}Si-^{29}Si CP-INADEQUATE CPMG	5.6	10	384x48	12x15	1743
1D ^{29}Si Direct Excitation	3600	10	144	-	8640

[a] For 2D NMR spectra, the first number indicates the number of scans and the second number indicates the number of indirect dimension points that were acquired.

[b] The first number indicates the number of rotor cycles per half echo and the second number indicates the total number of echoes acquired.

[c] The forward CP contact time was set to 6.5 ms, which was experimentally optimized.

[d] The spin rate of 22.22222 kHz was chosen to give a rotor echo delay of 45 μs.

Description of Computational Structures:

The hydrogen terminated Si-NS structures were obtained by taking a single layer of a Si backbone in $CaSi_2$, removing all Ca atoms, and adding hydrogen atoms on the above and below the appropriate Si atoms (see Figure S24a); vacuum spacing was not introduced between layers.

Raman, FTIR, Extinction Coefficient, Bands, and Orbitals:

The sheets on which Raman and FTIR calculations were performed are described below (also see Figure S24):

- **Silicane**: an infinite sheet of silicane with a unit cell formula of Si_2H_2
  - Unit cell consists of 1x2x1 Si atoms
- **cis-Hydroxysilicane**: an infinite sheet of cis-hydroxysilicane with a unit cell formula of Si_2H_2O
  - Unit cell consists of 1x2x1 Si atoms
- **cis-Chlorosilicane**: an infinite sheet of cis-chlorosilicane with a unit cell formula of Si_2HCl
  - Unit cell consists of 1x2x1 Si atoms
- **Si_8H_7Cl**: an infinite sheet of silicane with one hydrogen replaced with a chlorine with a unit cell formula of Si_8H_7Cl
  - Unit cell consists of 4x2x1 Si atoms
- **$(SiH_2(SiH)_2SiH_2)_4$**: a semi-infinite nanosheet that consists of periodic $SiH_2(SiH)_2SiH_2$ groups in only one direction
  - Unit cell consists of 8x2x1 Si atoms

The VASP POSCAR and relevant output files have been included with the Supporting Information as a zipped archive.

Solid State NMR:

The three finite sheets are described in the following (see Figure S30):

- **NMR 1**: a sheet of pure silicane with a chemical formula of $Si_{72}H_{96}$ (i.e., $(SiH)_{50}(SiH_2)_{20}(SiH_3)_2$)
- **NMR 2**: the sheet of **NMR 1** with a hydrogen near the center of the sheet replaced with a chlorine atom, having a chemical formula of $Si_{72}H_{95}Cl$ (i.e., $(SiH)_{49}(SiCl)(SiH_2)_{20}(SiH_3)_2$)
- **NMR 3**: the sheet of **NMR 2** with the chlorine atom replaced with a hydroxyl group, having a chemical formula of $Si_{72}H_{96}O$ (i.e., $(SiH)_{49}(SiOH)(SiH_2)_{20}(SiH_3)_2$)

The four infinite sheet models are described in the following (see Figure S31):

- **NMR 4**: a sheet of silicane with a unit cell formula of Si_2H_2
- **NMR 5**: a sheet of cis-hydroxysilicane with a unit cell formula of Si_2H_2O
- **NMR 6**: a sheet of cis-chlorosilicane with a unit cell formula of Si_2HCl
- **NMR 7**: a sheet of silicane with one chlorine replaced with a hydrogen with a unit cell formula of Si_8H_7Cl

The CASTEP NMR output and structure files have been included in the Supporting Information as a zipped archive.

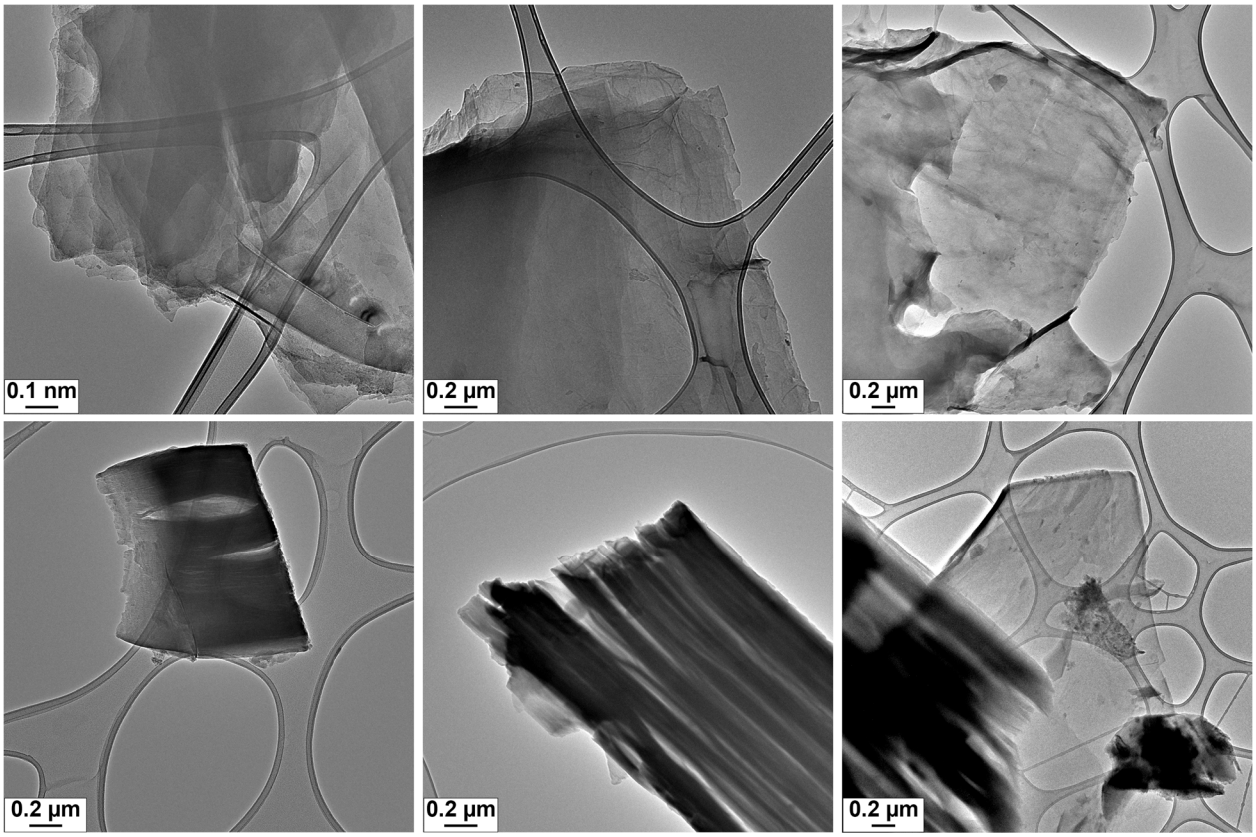

Figure S1. TEM images of the Si-NSs emphasizing their sheet-like morphology.

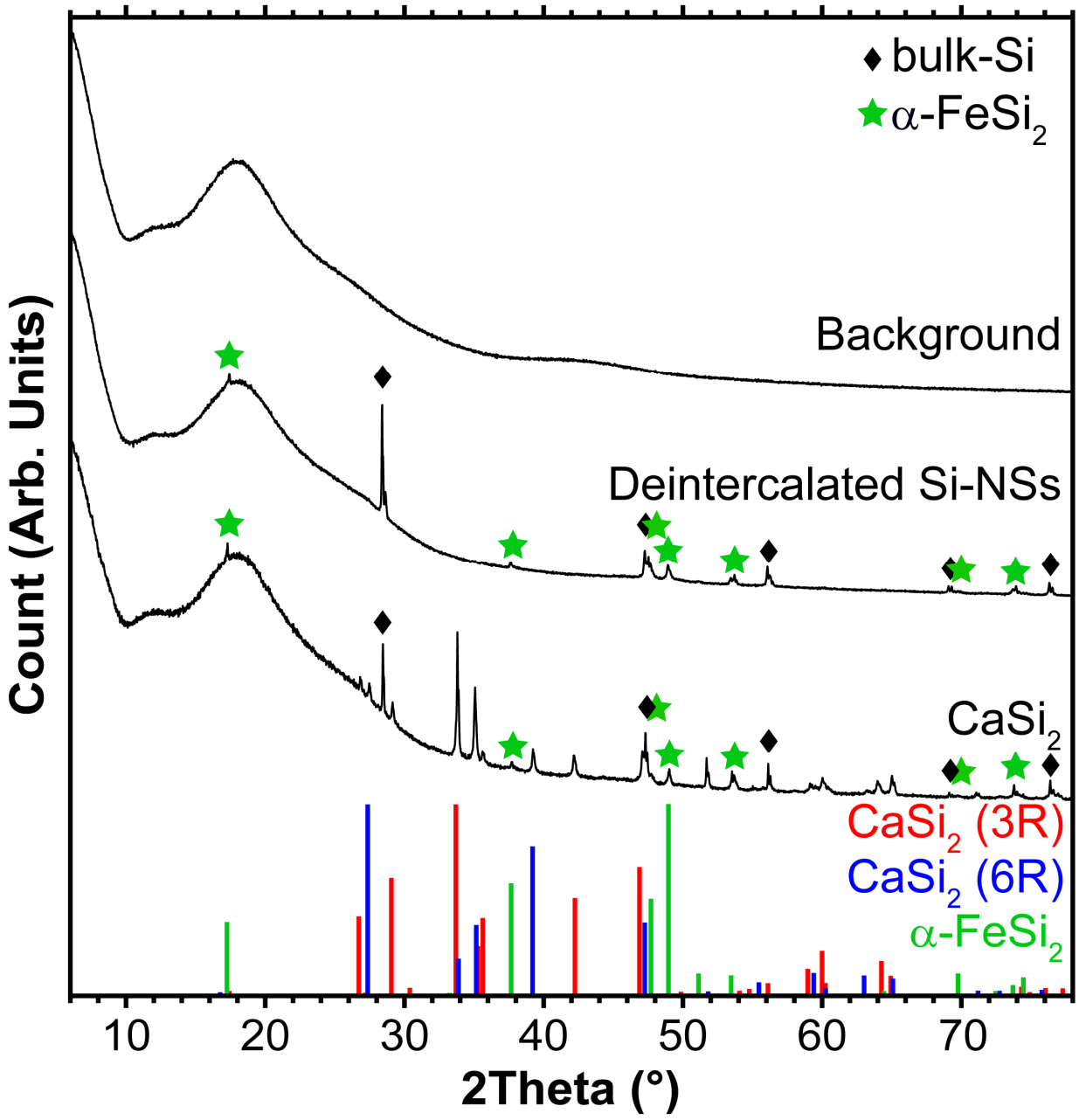

Figure S2. XRD of the purchased $CaSi_2$ precursor, Si-NSs, and the background. XRD references of $CaSi_2$ (3R), $CaSi_2$ (6R), and α-$FeSi_2$ correspond to PDF#04-013-6746, PDF#01-083-6182, and PDF#00-035-0822, respectively.

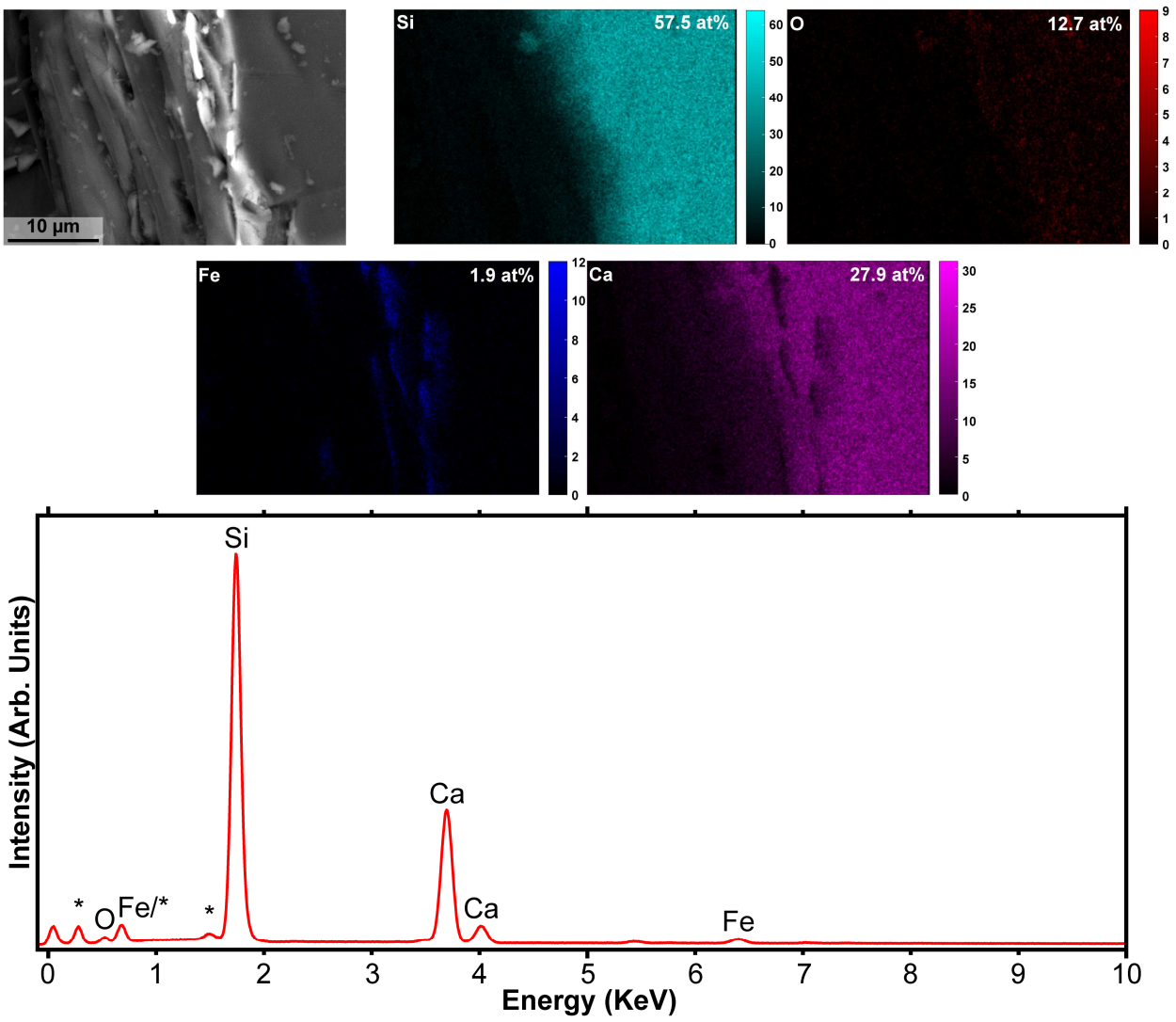

Figure S3. SEM image (top left), EDS mapping (upper), and associated EDS spectrum (lower) of the $CaSi_2$ precursor. In the EDS maps, the element and overall atomic percent are indicated, respectively, at the top left and top right of each image. In the EDS spectrum, all peaks labeled with a * are artifacts of the background; the peaks at ca. 0.3, 0.7, and 1.5 KeV correspond to carbon from the carbon paint used to affix the sample to the sample stage, fluorine from the fluoroelastomer in the carbon paint, and aluminum from the sample stage, respectively (see Figure S11-Figure S13 for SEM and EDS of the carbon paint and sample stage). All colors for the EDS maps were scaled equivalently, regardless of the atomic percent. All scale bars are in units of counts.

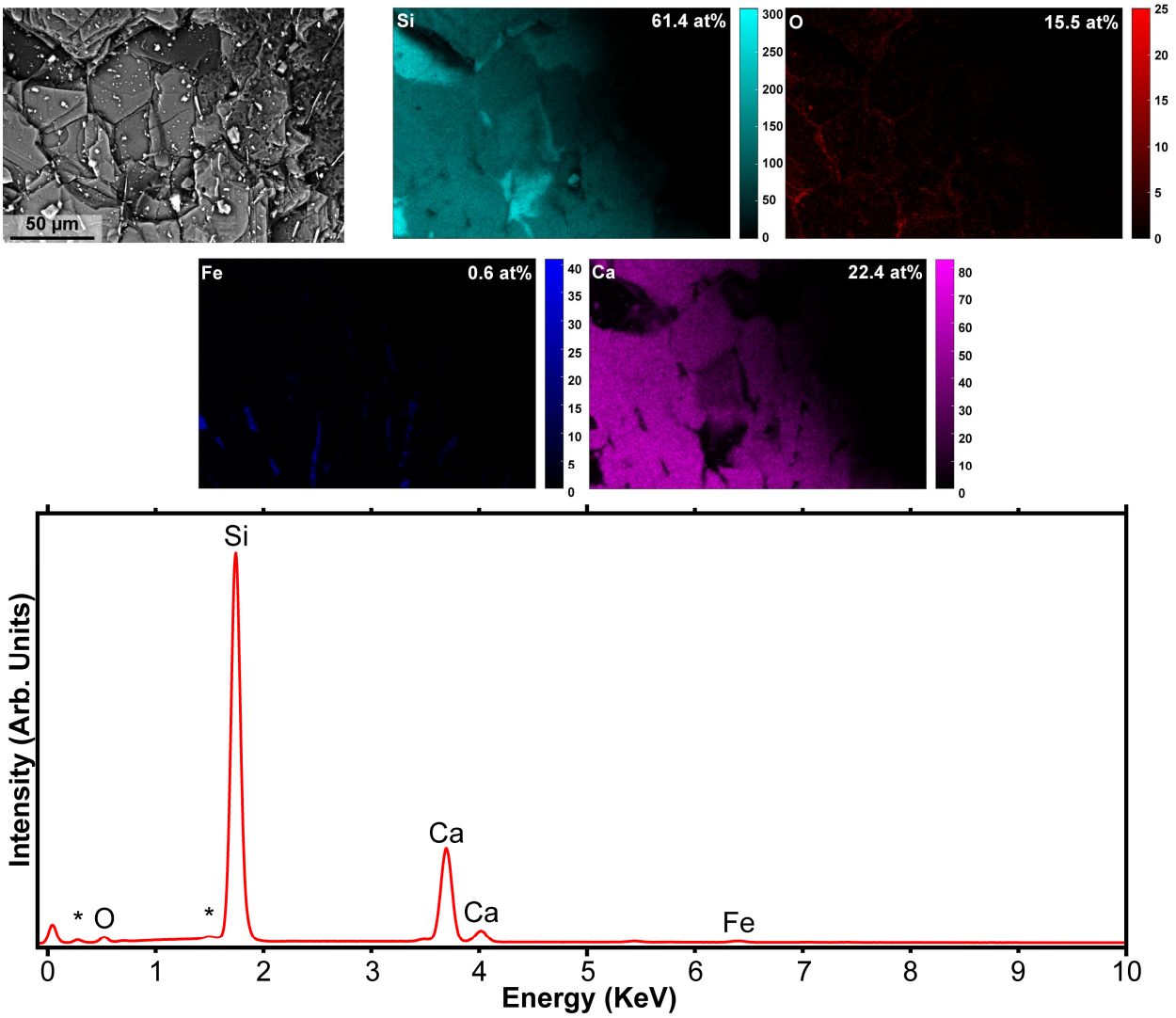

Figure S4. SEM image (top left), EDS mapping (upper), and associated EDS spectrum (lower) of the $CaSi_2$ precursor. In the EDS maps, the element and overall atomic percent are indicated, respectively, at the top left and top right of each image. In the EDS spectrum, all peaks labeled with a * are artifacts of the background; the peaks at ca. 0.3 and 1.5 KeV correspond to carbon from the carbon paint used to affix the sample to the sample stage and aluminum from the sample stage, respectively (see Figure S11-Figure S13 for SEM and EDS of the carbon paint and sample stage). All colors for the EDS maps were scaled equivalently, regardless of the atomic percent. All scale bars are in units of counts.

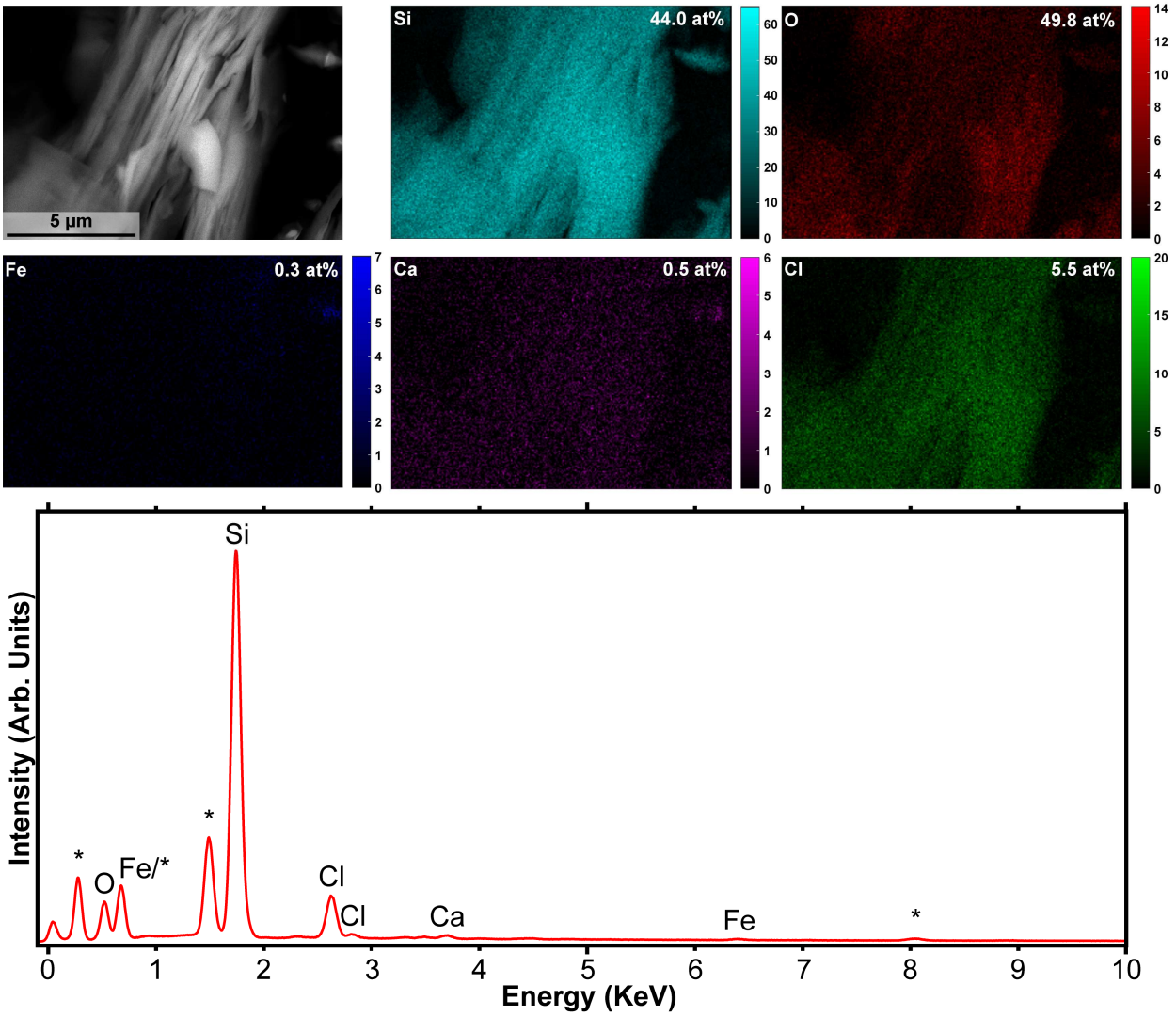

Figure S5. SEM image (top left), EDS mapping (upper), and associated EDS spectrum (lower) of the Si-NSs. In the EDS maps, the element and overall atomic percent are indicated, respectively, at the top left and top right of each image. In the EDS spectrum, all peaks labeled with * are artifacts of the background; the peaks at ca. 0.3, 0.7, 1.5, and 8.04 KeV correspond to carbon from the carbon paint used to affix the sample to the sample stage, fluorine from the fluoroelastomer in the carbon paint, aluminum from the sample stage, and copper from the sample stage, respectively (see Figure S11-Figure S13 for SEM and EDS of the carbon paint and sample stage). It is important to note that the oxygen signal is an absolute upper limit of Si-O, as intercalated H_2O and adsorbed O_2 from air exposure both contribute to the oxygen signal; further, the carbon paint has ~3 at% O. All colors for the EDS maps were scaled equivalently, regardless of the atomic percent. All scale bars are in units of counts. Data were collected 0.2 months after the Si-NSs were isolated.

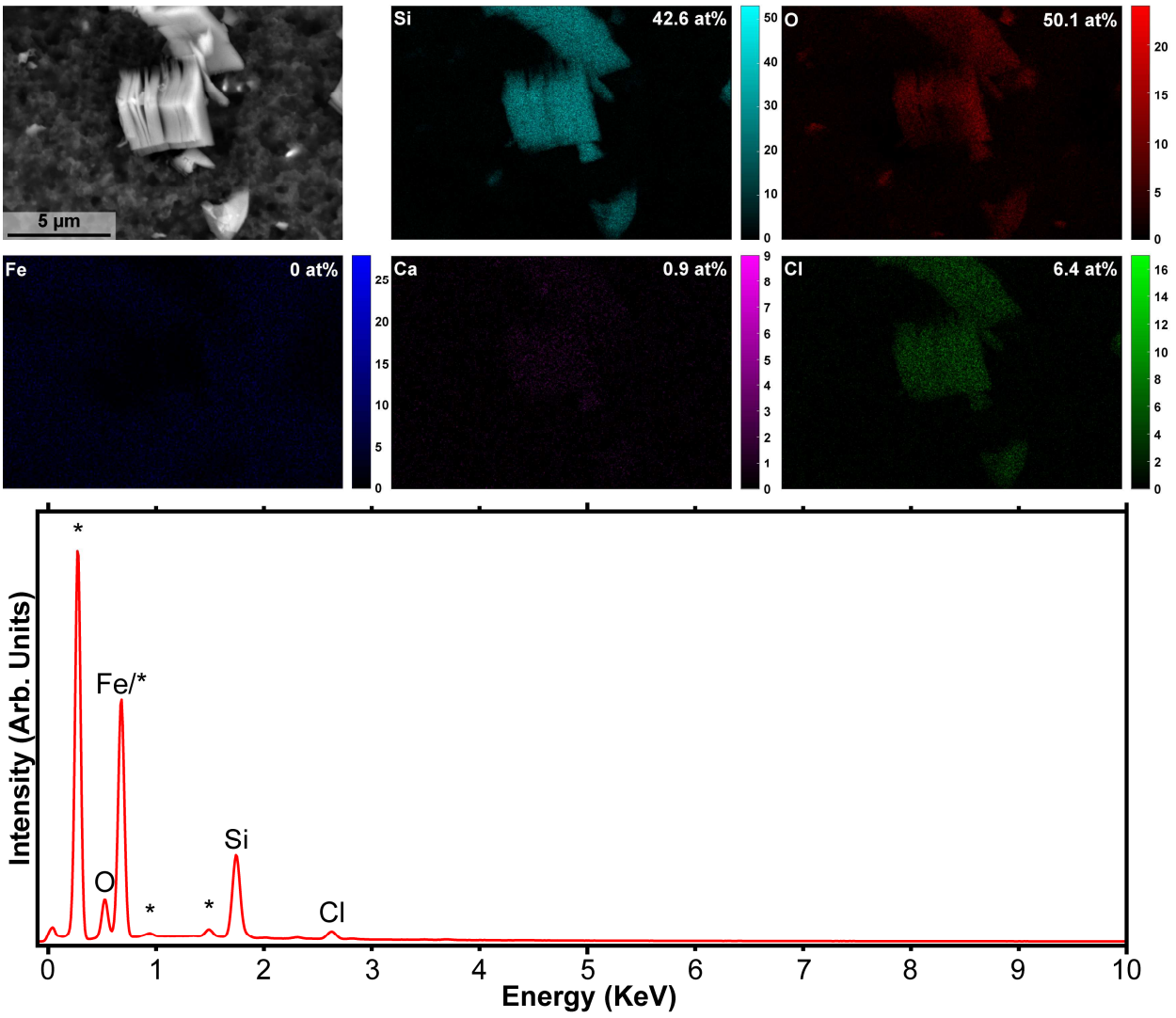

Figure S6. SEM image (top left), EDS mapping (upper), and associated EDS spectrum (lower) of the Si-NSs. In the EDS maps, the element and overall atomic percent are indicated, respectively, at the top left and top right of each image. In the EDS spectrum, all peaks labeled with * are artifacts of the background; the peaks at ca. 0.3, 0.7, 0.9, and 1.5 KeV correspond to carbon from the carbon paint used to affix the sample to the sample stage, fluorine from the fluoroelastomer in the carbon paint, copper from the sample stage, and aluminum from the sample stage, respectively (see Figure S11-Figure S13 for SEM and EDS of the carbon paint and sample stage). It is important to note that the oxygen signal is an absolute upper limit of Si-O, as intercalated H_2O and adsorbed O_2 from air exposure both contribute to the oxygen signal; further, the carbon paint has ~3 at% O. All colors for the EDS maps were scaled equivalently, regardless of the atomic percent. All scale bars are in units of counts. Data were collected 3.7 months after the Si-NSs were isolated.

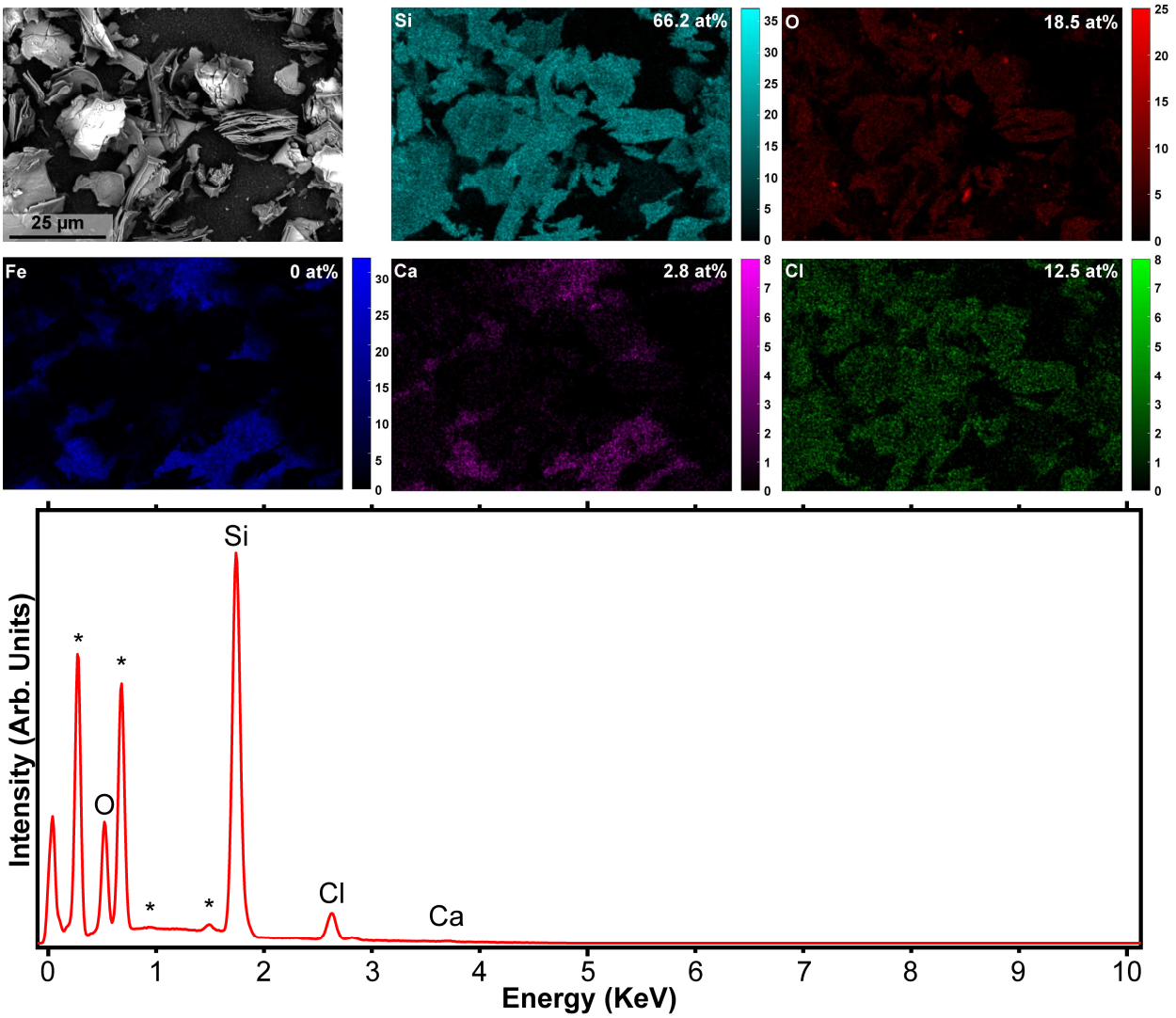

Figure S7. SEM image (top left), EDS mapping (upper), and associated EDS spectrum (lower) of the Si-NSs. In the EDS maps, the element and overall atomic percent are indicated, respectively, at the top left and top right of each image. In the EDS spectrum, all peaks labeled with * are artifacts of the background; the peaks at ca. 0.3, 0.7, 0.9, and 1.5 KeV correspond to carbon from the carbon paint used to affix the sample to the sample stage, fluorine from the fluoroelastomer in the carbon paint, copper from the sample stage, and aluminum from the sample stage, respectively (see Figure S11-Figure S13 for SEM and EDS of the carbon paint and sample stage). The few bright spots in the oxygen map correspond to Al_2O_3. It is important to note that the oxygen signal is an upper limit of Si-O, as intercalated H_2O and adsorbed O_2 from air exposure both contribute to the oxygen; further, the carbon paint has ~3 at% O. We hypothesize that this image has significantly less oxygen signal than those shown in Figure S5 and Figure S6 due to increased exfoliation, and thus less intercalated H_2O. All colors for the EDS maps were scaled equivalently, regardless of the atomic percent. All scale bars are in units of counts. Note that a majority of the Ca signal is coming from the background, and that the Ca and Cl signals are nearly mutually exclusive. Data were collected 1.4 months after the Si-NSs were isolated.

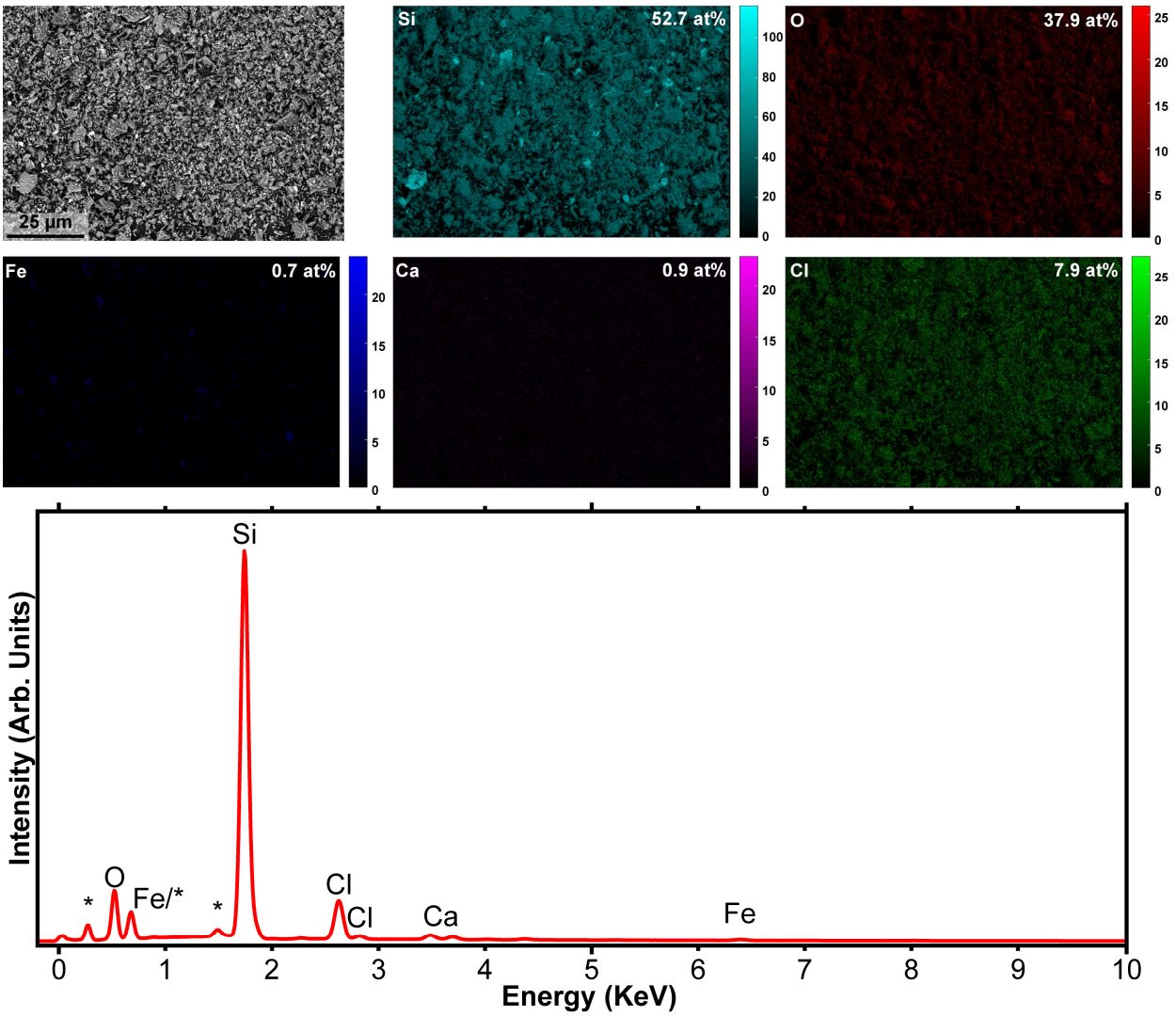

Figure S8. SEM image (top left), EDS mapping (upper), and associated EDS spectrum (lower) of the Si-NSs. In the EDS maps, the element and overall atomic percent are indicated, respectively, at the top left and top right of each image. In the EDS spectrum, all peaks labeled with * are artifacts of the background; the peaks at ca. 0.3, 0.7, and 1.5 KeV correspond to carbon from the carbon paint used to affix the sample to the sample stage, fluorine from the fluoroelastomer in the carbon paint, and aluminum from the sample stage, respectively (see Figure S11-Figure S13 for SEM and EDS of the carbon paint and sample stage). It is important to note that the oxygen signal is an upper limit of Si-O, as intercalated H_2O and adsorbed O_2 from air exposure both contribute to the oxygen signal; further, the carbon paint has ~3 at% O. All colors for the EDS maps were scaled equivalently, regardless of the atomic percent. All scale bars are in units of counts. Data were collected 3.7 months after the Si-NSs were isolated.

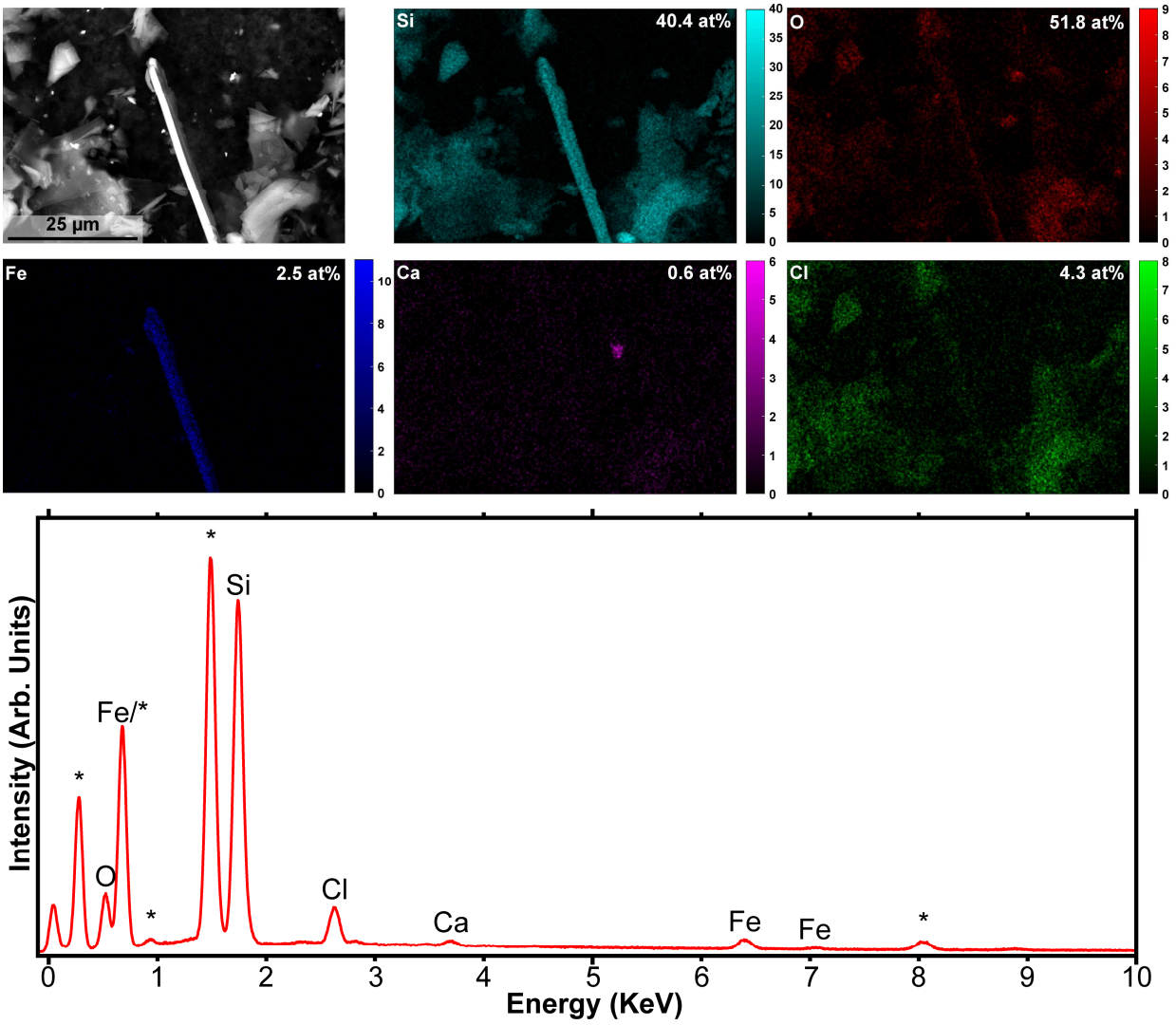

Figure S9. SEM image (top left), EDS mapping (upper), and associated EDS spectrum (lower) of the Si-NSs, showing the presence of iron silicide. In the EDS maps, the element and overall atomic percent are indicated, respectively, at the top left and top right of each image. In the EDS spectrum, all peaks labeled with * are artifacts of the background; the peaks at ca. 0.3, 0.7, 0.9, 1.5, and 8.04 KeV correspond to carbon from the carbon paint used to affix the sample to the sample stage, fluorine from the fluoroelastomer in the carbon paint, copper from the sample stage, aluminum from the sample stage, and copper from the sample stage, respectively (see Figure S11-Figure S13 for SEM and EDS of the carbon paint and sample stage). All colors for the EDS maps were scaled equivalently, regardless of the atomic percent. All scale bars are in units of counts. Data were collected 0.2 months after the Si-NSs were isolated.

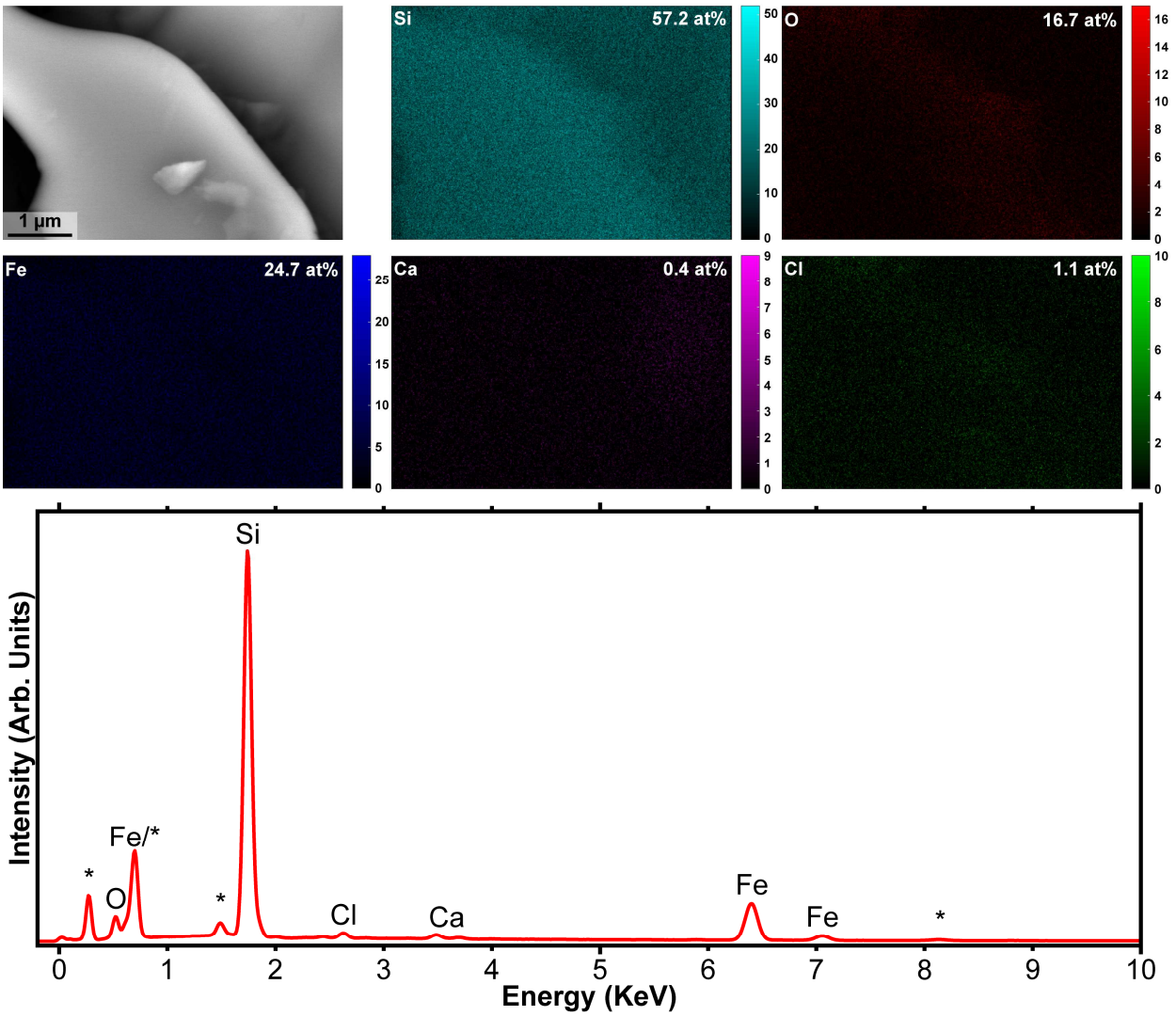

Figure S10. SEM image (top left), EDS mapping (upper), and associated EDS spectrum (lower) of the Si-NSs, showing the presence of iron silicide, with a total atomic ratio of Fe:Si = 2.3:1. In the EDS maps, the element and overall atomic percent are indicated, respectively, at the top left and top right of each image. In the EDS spectrum, all peaks labeled with * are artifacts of the background; the peaks at ca. 0.3, 0.7, 1.5, and 8.04 KeV correspond to carbon from the carbon paint used to affix the sample to the sample stage, fluorine from the fluoroelastomer in the carbon paint, aluminum from the sample stage, and copper from the sample stage, respectively (see Figure S11-Figure S13 for SEM and EDS of the carbon paint and sample stage). All colors for the EDS maps were scaled equivalently, regardless of the atomic percent. All scale bars are in units of counts. Data were collected 3.7 months after the Si-NSs were isolated.

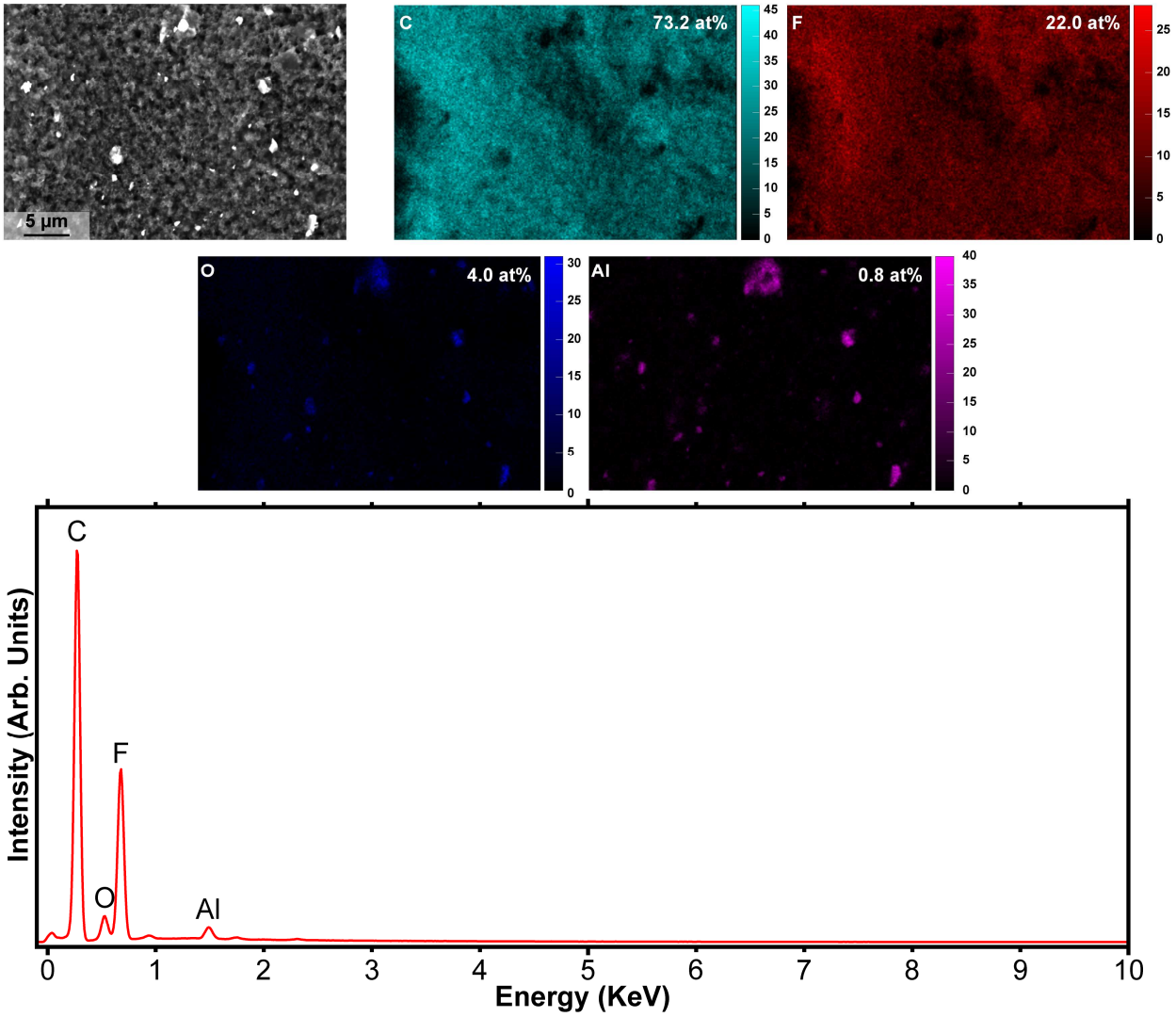

Figure S11. SEM image (top left), EDS mapping (upper), and associated EDS spectrum (lower) of the carbon paint used to affix the sample to the sample stage, showing the presence of F, Al, and O. All colors for the EDS maps were scaled equivalently, regardless of the atomic percent. All scale bars are in units of counts.

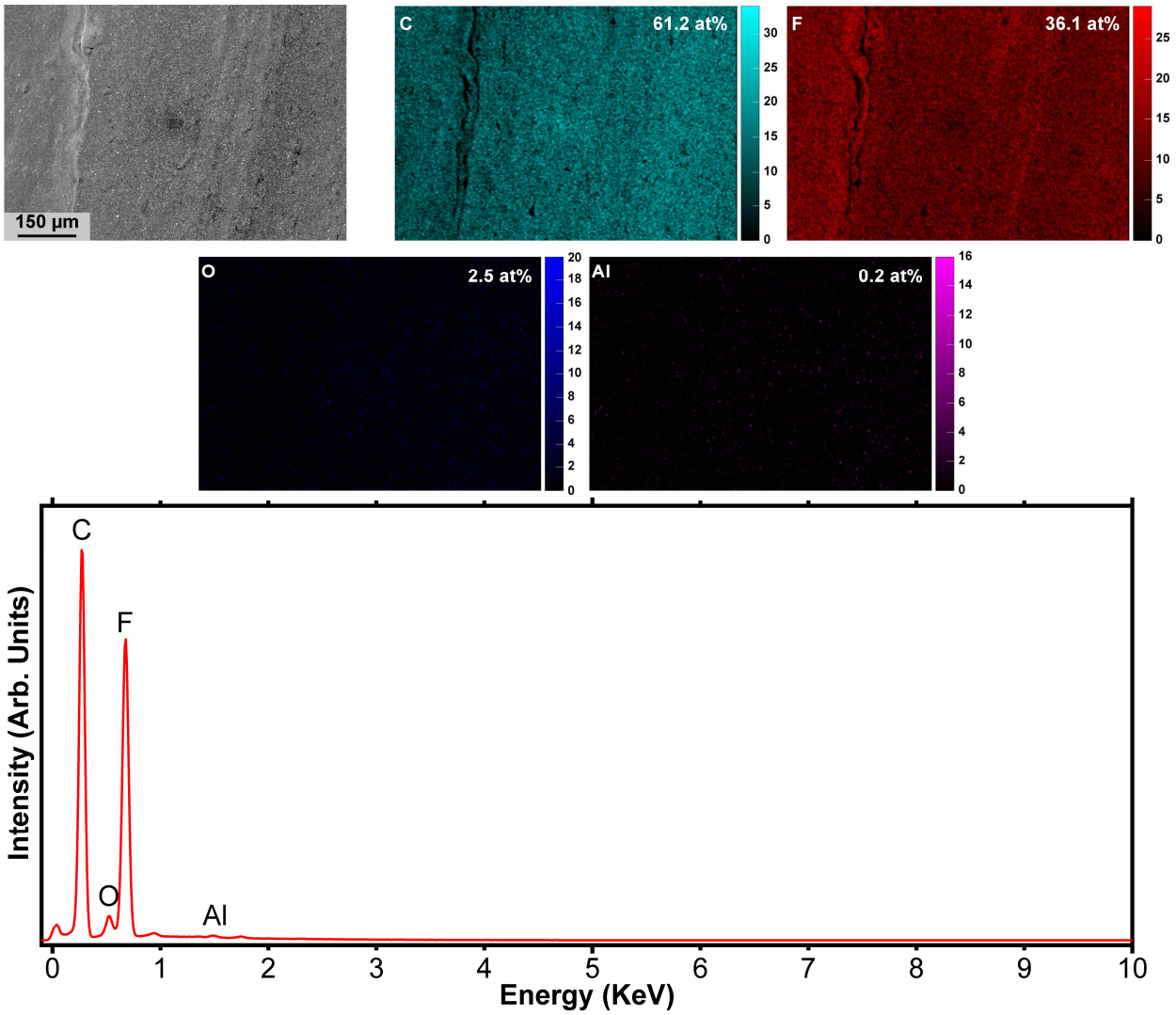

Figure S12. SEM image (top left), EDS mapping (upper), and associated EDS spectrum (lower) of the carbon paint used to affix the sample to the sample stage. Darkened portion of the SEM image is an artifact of the image process from Figure S11. All colors for the EDS maps were scaled equivalently, regardless of the atomic percent. All scale bars are in units of counts.

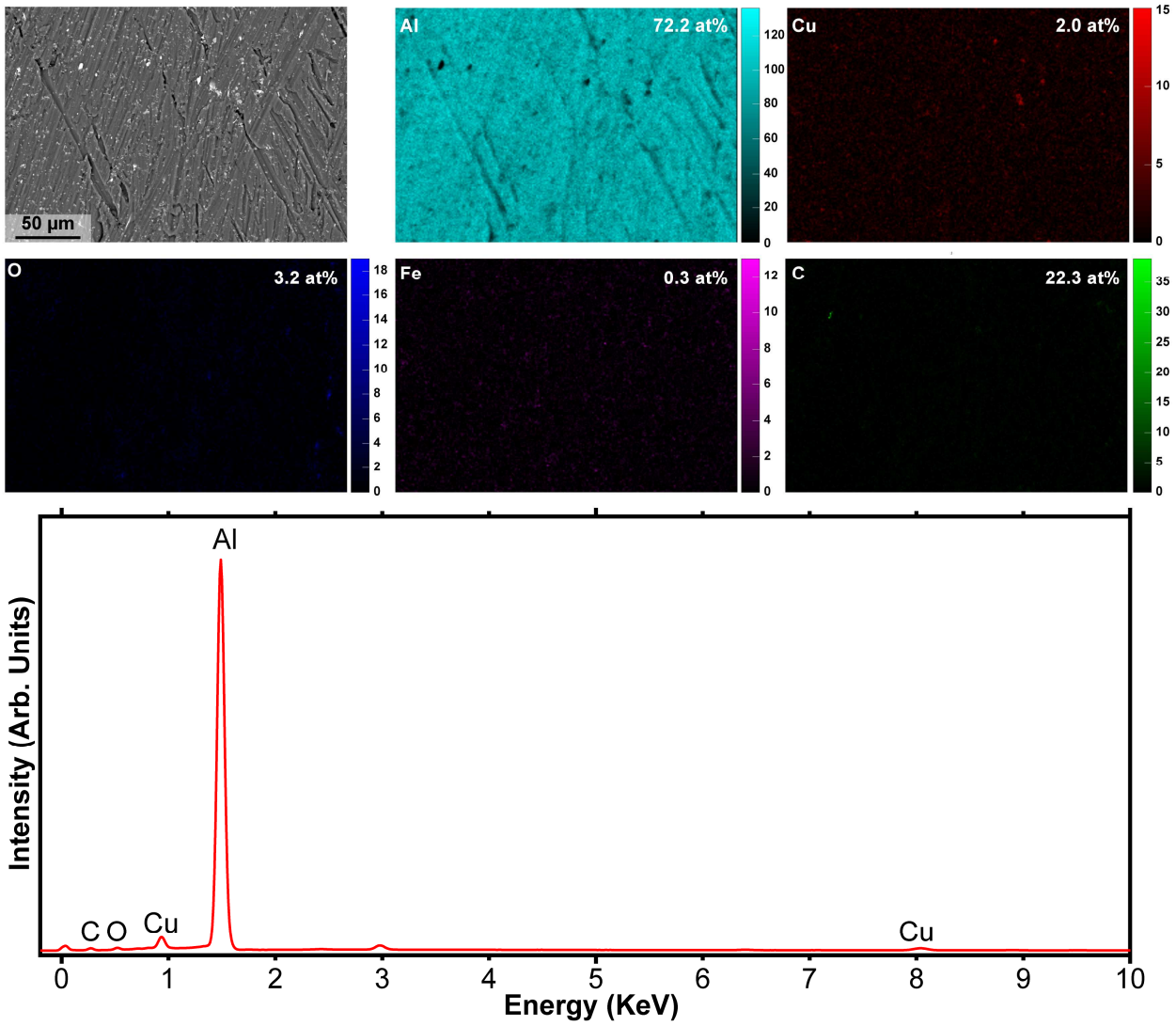

Figure S13. SEM image (top left), EDS mapping (upper), and associated EDS spectrum (lower) of the sample stage on which the sample (from Figure S3-Figure S12) was affixed, showing the presence of the Cu and Cl. All colors for the EDS maps were scaled equivalently, regardless of the atomic percent. All scale bars are in units of counts.

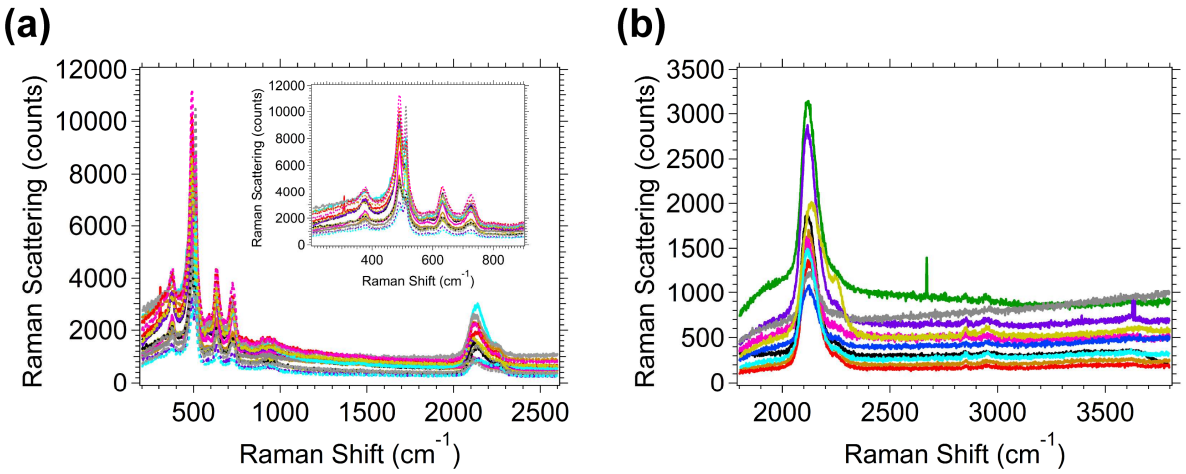

Figure S14. Replicate Raman spectra of the Si-NSs in the (a) low-wavenumber region and (b) high-wavenumber region. The color traces represent individual Raman spectra acquired at different locations on the sample (a) 18 locations and (b) 10 locations.

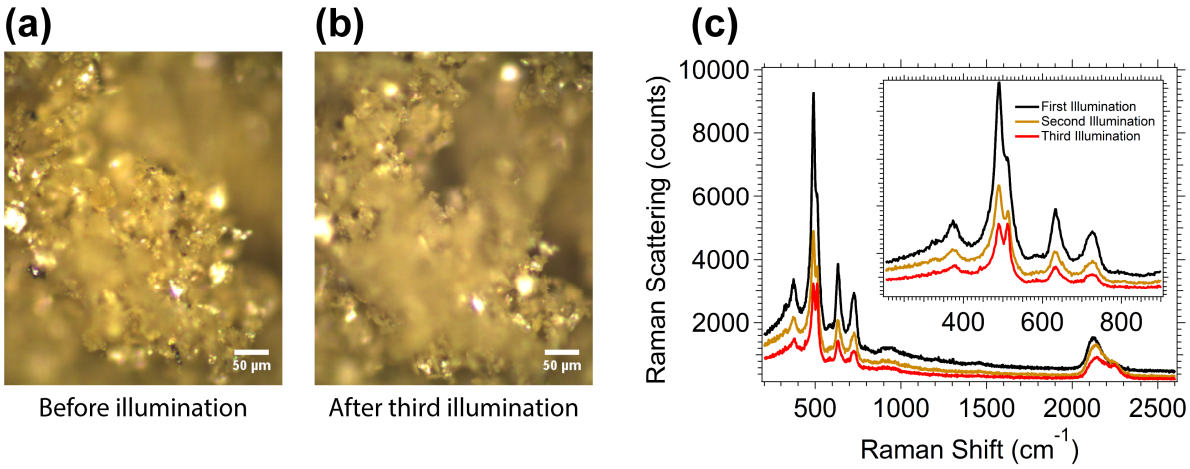

Figure S15. Bright-field optical microscopy images of the Si-NSs (a) before and (b) after illumination with the Raman laser for 3 minutes. Panel (c) shows three replicate Raman spectra collected at the same location. Each spectrum was collected with a 1-minute acquisition time. With increasing illumination time, there is a decrease in the relative intensity of the peak at ~489 cm^{-1} compared to the peak at ~511 cm^{-1}. This suggests that the 2D Si_6 framework loses its phonon modes while the bulk-Si impurities remain unchanged.

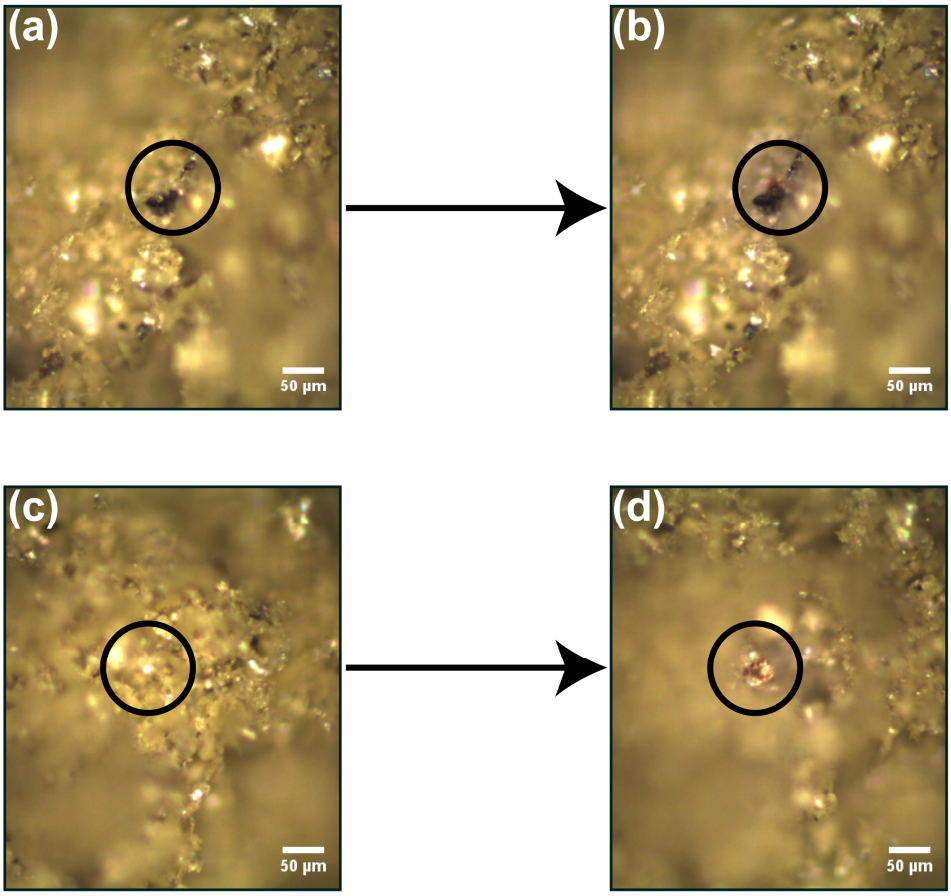

Figure S16. Bright-field optical microscopy images showing the visual changes induced by illumination with the Raman laser. We note that the physical appearance of the Si-NSs changes at high laser powers with 532 nm excitation. When collecting Raman data at laser powers greater than 1.42×10^4 W cm^{-2}, the sample began to change color from yellow to red-brown. It is unclear what exactly causes discoloration of the Si-NSs upon laser radiation; however, previous literature reports suggest that this red color is a result of the formation of siloxenes.[15–18] Additionally, bright-field optical microscopy images collected after illumination also show that the product takes on a dull grey appearance, which is expected to be oxidation to SiO-containing species. During laser exposure, we observe a decreasing SiH_n peak at 2126 cm^{-1} with an increasing $OSiH_n$ peak at 2250 cm^{-1}, suggesting the sample oxidizes during exposure to the high-power laser.

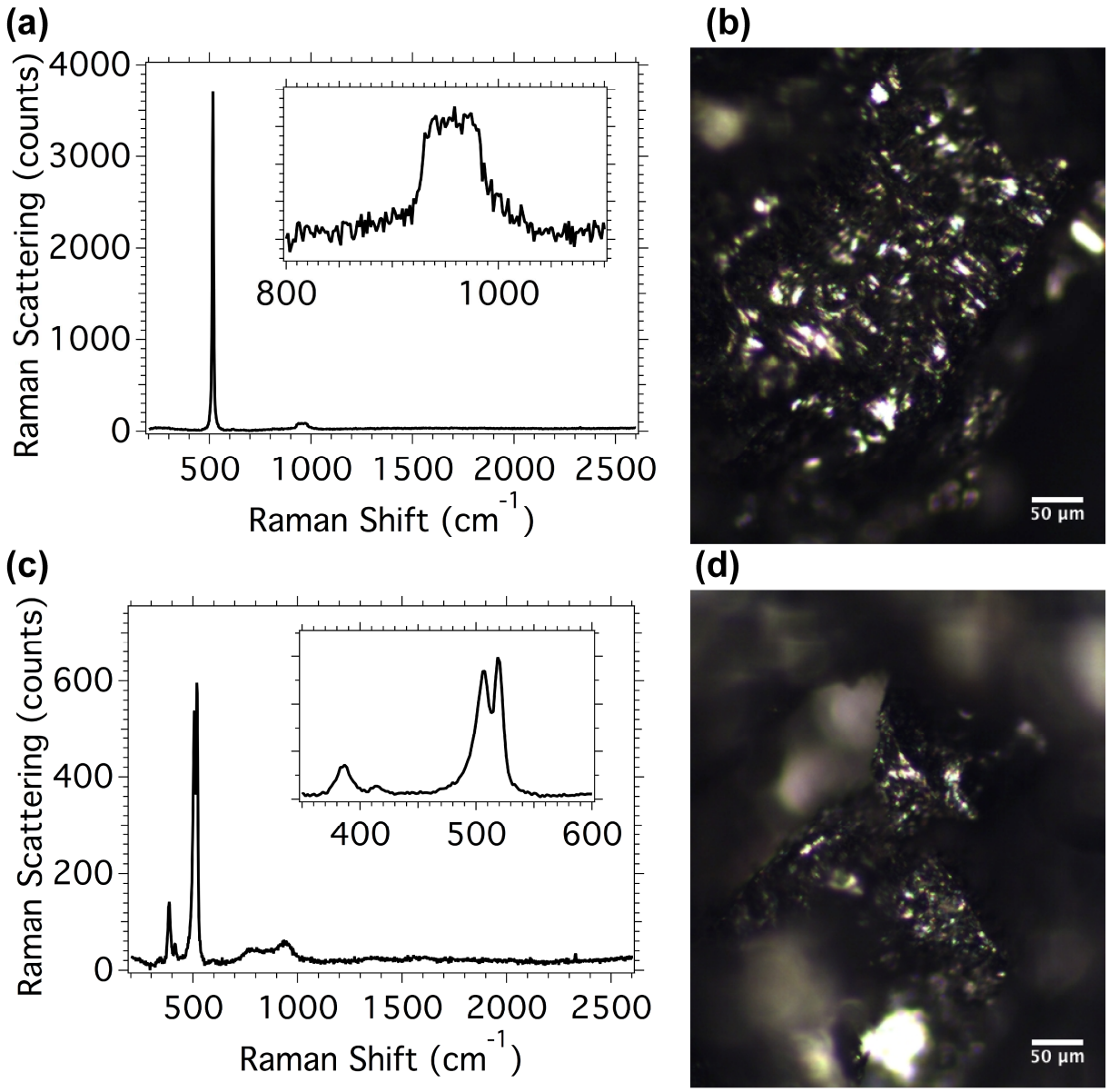

Figure S17. Raman spectra of the $CaSi_2$ precursor clearly indicating the presence of bulk-Si (a, b) and $CaSi_2$ (c, d). Bright-field optical microscopy images corresponding to the location of the sample from which the Raman data were collected.

Table S2. Raman active vibrational modes of the Si-NSs.

Wavenumber (cm^{-1}) Experimental	Wavenumber (cm^{-1}) DFT[a]	Wavenumber (cm^{-1}) Literature[b]	Assignment	Reference
~335*	343	-	Simultaneous SiSi, SiH, and SiCl	-
375	386	380-384	SiSi	19–21
489	483	485/470-495	SiSi	19,21
511	-	515	bulk-Si	22–25
~585*	565	-	SiH	-
632	616	640	SiH_n[c]	43, 48
~658*	659	-	SiH	-
726	724	~ 730	SiH	27
~900	897/910	-	SiH_2/SiOH	-
~945	-	~960	bulk-Si	23–25
2126	2131	2000-2120 or 2163	SiH_n[c]	26–28
2248	-	2250	$OSiH_n$	29

[a] DFT calculations were performed in this work.

[b] Literature assignments correspond to reference column.

[c] SiH_n groups include monohydrides, dihydrides, and trihydrides.

*Groups with this label were omitted from the main text Figure 2 as their intensity is very low.

Note that the peak at 511 cm^{-1} is red shifted due to the neighboring high intensity peak at 489 cm^{-1}.

Table S3. FTIR active vibrational modes of the Si-NSs.

Wavenumber (cm^{-1}) Experimental	Wavenumber (cm^{-1}) DFT[a]	Wavenumber (cm^{-1}) Literature[b]	Assignment	Reference
512	511	514	SiH	30
571.8	547	565	SiCl	31
634.5	601	640	SiH	37, 54, 55
742	-	740	SiH	21
797.4	773	800	SiO	30
876.5	-	870	SiH_2	37, 43
897	897/903	885	SiH_2/SiOH[c]	32
1026.9	-	1060	SiOSi	43, 55
1389.5	-	1359	C-H	-
1456	-	1458	CH_x	-
1630.5	-	1635-1640	H_2O	-
2107.8	2136	2100	Si_3SiH	43, 55
2250.5	-	2250	O_3SiH	43, 55
2841.6	-	2853	CH_3	-
2944.8	-	2918	CH_x	-
2974.7	-	2965	CH_3	-
3362.3	-	3302 - 3446	H_2O	-
3595	3741	3685	SiOH	34

[a] DFT calculations were performed in this work.

[b] Literature assignments correspond to reference column.

Table S4. Raman active vibrational modes of the $CaSi_2$ precursor.

Raman Shift (cm^{-1}) Experimental	Raman Shift (cm^{-1}) DFT	Raman Shift (cm^{-1}) Literature[a]	Assignment	Reference
343	-	349	A_{1g}(Si2) of $CaSi_2$	35
387	-	387	A_{1g}(Si1) of $CaSi_2$	35
413	-	416	E_g(Si2) of $CaSi_2$	35
506	-	515	2D-Si of $CaSi_2$	35
519	-	520	bulk-Si	41, 43
956	-	~960	bulk-Si	41, 43

[a] Literature assignments correspond to reference column.

Table S5. Table of Born effective charge tensors (in arbitrary units) used to compare relative peak intensities of SiO and SiH bonds.

Ion Number	Element	-	-	-
		α-Quartz		
1	Si	2.9936	-3E-05	1E-5
		0.00017	3.70172	-0.25976
		2E-05	0.22109	3.45115
2	Si	3.52466	0.30651	0.22498
		0.30669	3.17065	0.12989
		-0.19145	-0.11051	3.45112
3	Si	3.52468	-0.30673	-0.22494
		-0.30656	3.17069	0.12988
		0.19151	-0.11056	3.45116
4	O	-1.32255	0.54398	0.37705
		0.49839	-2.02499	-0.74867
		0.33043	-0.78237	-1.72556
5	O	-2.30088	-0.06604	0.83675
		-0.02058	-1.04684	0.0478
		0.84271	0.10503	-1.72551
6	O	-1.39807	-0.54196	0.45984
		-0.5876	-1.94961	0.70089
		0.51231	0.67732	-1.72559
7	O	-1.39787	0.54198	-0.45978
		0.58737	-1.94985	0.70074
		-0.51233	0.6773	-1.72559
8	O	-2.30073	0.06637	-0.83687
		0.02079	-1.04685	0.04782
		-0.84275	0.10503	-1.7256
9	O	-1.32285	-0.54409	-0.37704
		-0.49867	-2.02492	-0.74858
		-0.33045	-0.78233	-1.72559
		cis-Hydroxysilicane		
1	Si	1.09389	0	-3.00E-05
		0	1.02181	-0.00272
		-1.00E-05	0.04637	1.23176
2	Si	-0.40153	-1.00E-05	1.00E-05
		0	-0.32912	0.01077
		1.00E-05	-0.012	0.27416
3	H	-0.31412	0	1.00E-05
		0	-0.24227	-0.00718
		1.00E-05	-0.02049	-0.29091
4	H	0.51166	-1.00E-05	1.00E-05
		2.00E-05	0.29211	0.06249
		0	-0.01179	0.59755
5	O	-0.88991	1.00E-05	0
		-1.00E-05	-0.74253	-0.06336
		-1.00E-05	-0.00209	-1.81256
		Silicane		
1	Si	0.39265	1.00E-05	-1.00E-05
		-1.00E-05	0.39256	2.00E-05
		-1.00E-05	1.00E-05	0.30722
2	Si	0.3925	0	1.00E-05
		1.00E-05	0.39258	-2.00E-05
		1.00E-05	-1.00E-05	0.30755
3	H	-0.39262	0	1.00E-05
		0	-0.39261	-2.00E-05
		0	0	-0.30733
4	H	-0.39252	0	-1.00E-05
		0	-0.39253	3.00E-05
		0	0	-0.30744

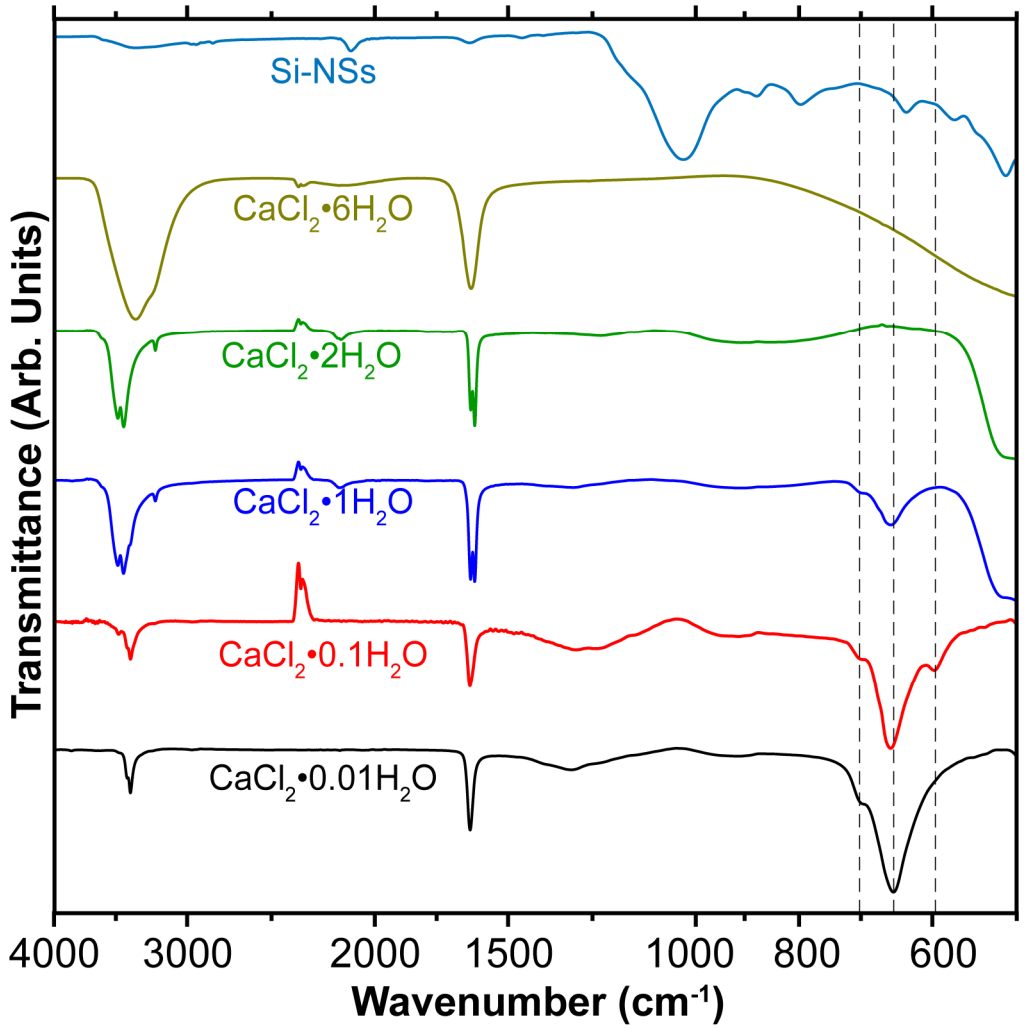

Figure S18. FTIR of various nominal calcium chloride hydrates. Samples were prepared by drying $CaCl_2 \cdot 2H_2O$ at ~450 °C, then hydrating with a prescribed amount of water. The concave-down peak at ~2350 cm^{-1} is a result of an over subtraction of atmospheric CO_2. Dashed lines are to guide the eye. Note that the x-axis is plotted on log scale, increasing the apparent width of all peaks in the fingerprint region while compressing the width of all peaks at high wavenumber.

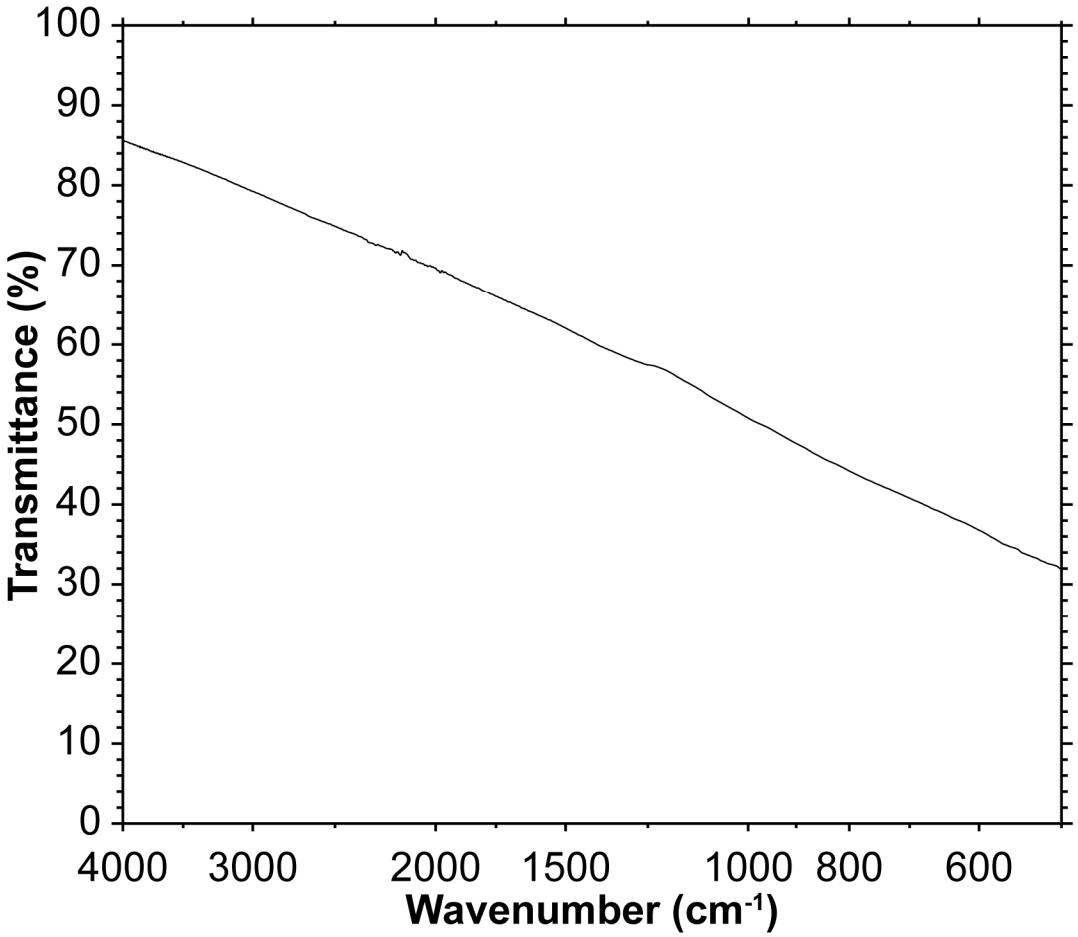

Figure S19. FTIR spectra of the $CaSi_2$ precursor. Note that the x-axis is plotted on log scale. Background subtraction was not performed. Background subtraction was not performed on any FTIR data in this manuscript.

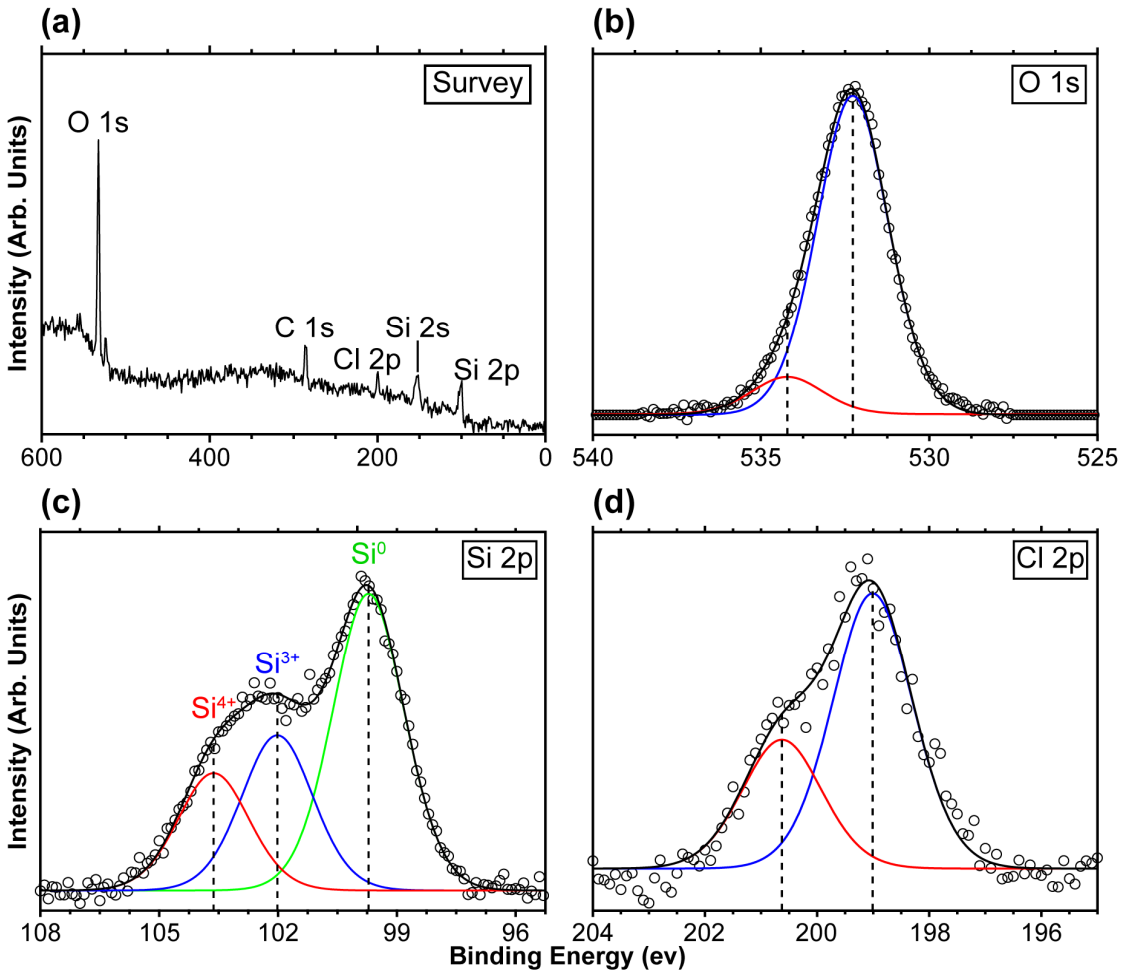

Figure S20. XPS of the Si-NSs. In panels (b)-(c), the black open circles correspond to the experimental data, while the solid black line is the sum of the peak fits. Time-dependent studies on the oxidation of silicane are needed, but are outside the scope of this work. Note that this data were collected 10.8 months after the Si-NSs were isolated.

To further characterize the oxidation state of the Si-NSs, XPS data were collected (Figure S20). The Si 2p peaks can be deconvoluted into three peaks with binding energies of 99.7, 102.0, and 103.6 eV, which are assigned to oxidation states of Si^0, Si^{3+}, and Si^{4+}, respectively;[36] however, we note that studies which specifically study XPS of the Si-NSs are scarce, which makes peak assignment difficult. Further, the DFT implemented in this work cannot model XPS because DFT does not explicitly model core electrons—the electrons which XPS probes. We thus conclude that XPS studies of this material system should be a topic of future research. XPS data were fit to a Gaussian Lorentz Product (GLP) function:

$$\mathbf{GLP(I, m = 30, E, FWHM)} = \mathbf{I} * \exp\left(-4\ln(2) * \left(1 - \frac{\mathbf{m}}{\mathbf{100}}\right) * \left(\frac{\mathbf{x - E}}{\mathbf{FWHM}}\right)^2\right) * \left(1 + \frac{\mathbf{4 * m}}{\mathbf{100}} * \left(\frac{\mathbf{x - E}}{\mathbf{FWHM}}\right)^2\right)^{-1} \quad \text{(S1)}$$

Table S6. Peak fitting parameters corresponding to the curves in Figure S20; parameters were determined by minimizing the sum of squared residuals.

E (eV)	FWHM (eV)	I	Area (%)
O 1s			
532.3	2.6	0.96	90.3
534.2	2.6	0.10	9.7
Si 2p			
99.7	2.21	0.91	52.2
102.0	2.21	0.47	27.2
103.6	2.21	0.36	20.6
Cl 2p			
199.0	1.75	0.80	68.2
200.6	1.75	0.37	31.8

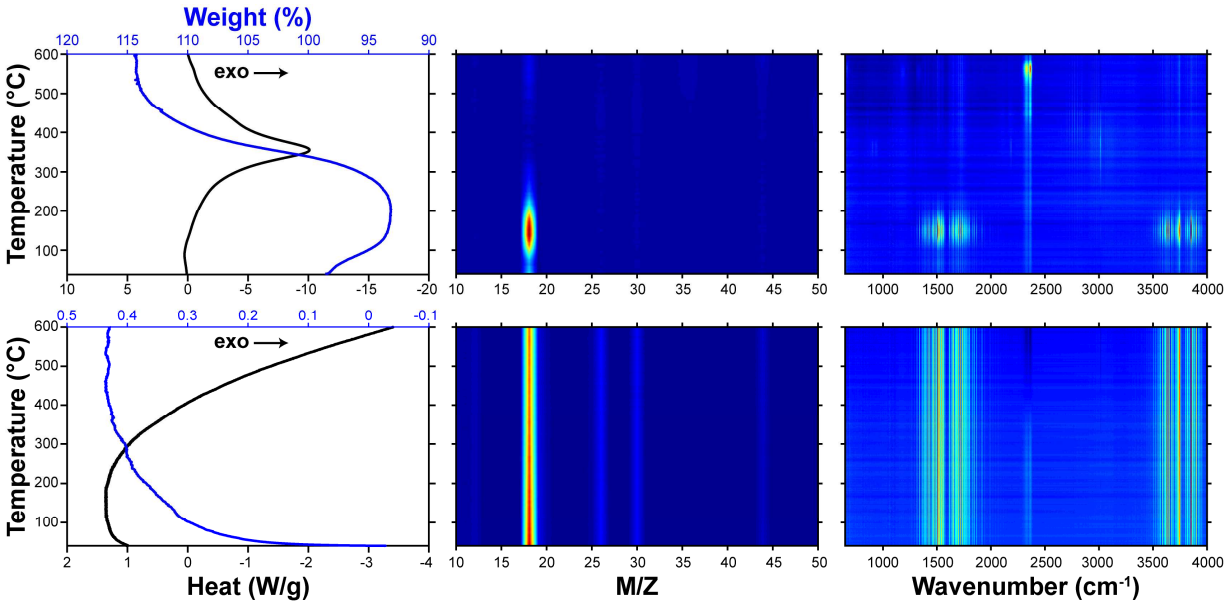

Figure S21. TGA and DSC (left), MS (middle), and FTIR (right) in air. FTIR peaks of CO_2 are likely due to the combustion of CH_x.

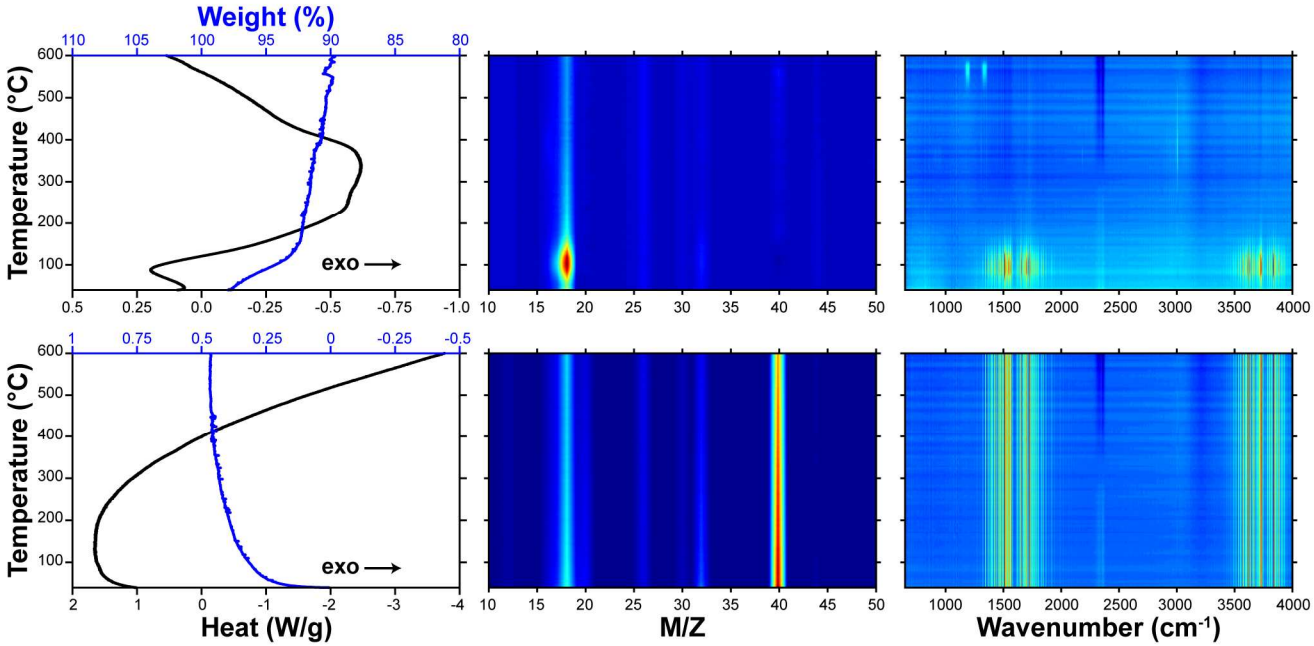

Figure S22. TGA and DSC (left), MS (middle), and FTIR (right) in nitrogen. FTIR peaks at ~1175 cm^{-1} and ~1325 cm^{-1} are likely due to the loss of CH_x.

The thermal decomposition of the Si-NSs was investigated with TGA and DSC, while the gaseous decomposition products were simultaneously monitored with FTIR and MS. Decomposition data were collected in both N_2 and synthetic air. An endothermic (+0.62 J) loss of water at ~100 °C with a mass loss of 5.2% suggests the presence of water; the energy to vaporize the same mass of water at 100 °C is +0.72 J. We note that condensation reactions of *SiH and *SiOH which liberate water are also a possibility. An exothermic loss of $HCl_{(g)}$ is observed between ~300-450 °C is observed. Potential H losses leave undetected and can only be inferred from TGA. It is unclear whether the source of HCl arises from condensation reactions of *SiCl and *SiH, or intercalated HCl. Data collected in N_2 (air) demonstrates ~10% (~15%) mass loss (increase) while theoretical loss of all hydrogens for infinite Si-NSs is 3.4%. XRD of the sample after running TGA/DSC (Figure S23) strongly resembles the original Si-NSs (Figure S2), despite the products appearing black and grey for samples run under N_2 and air, respectively.

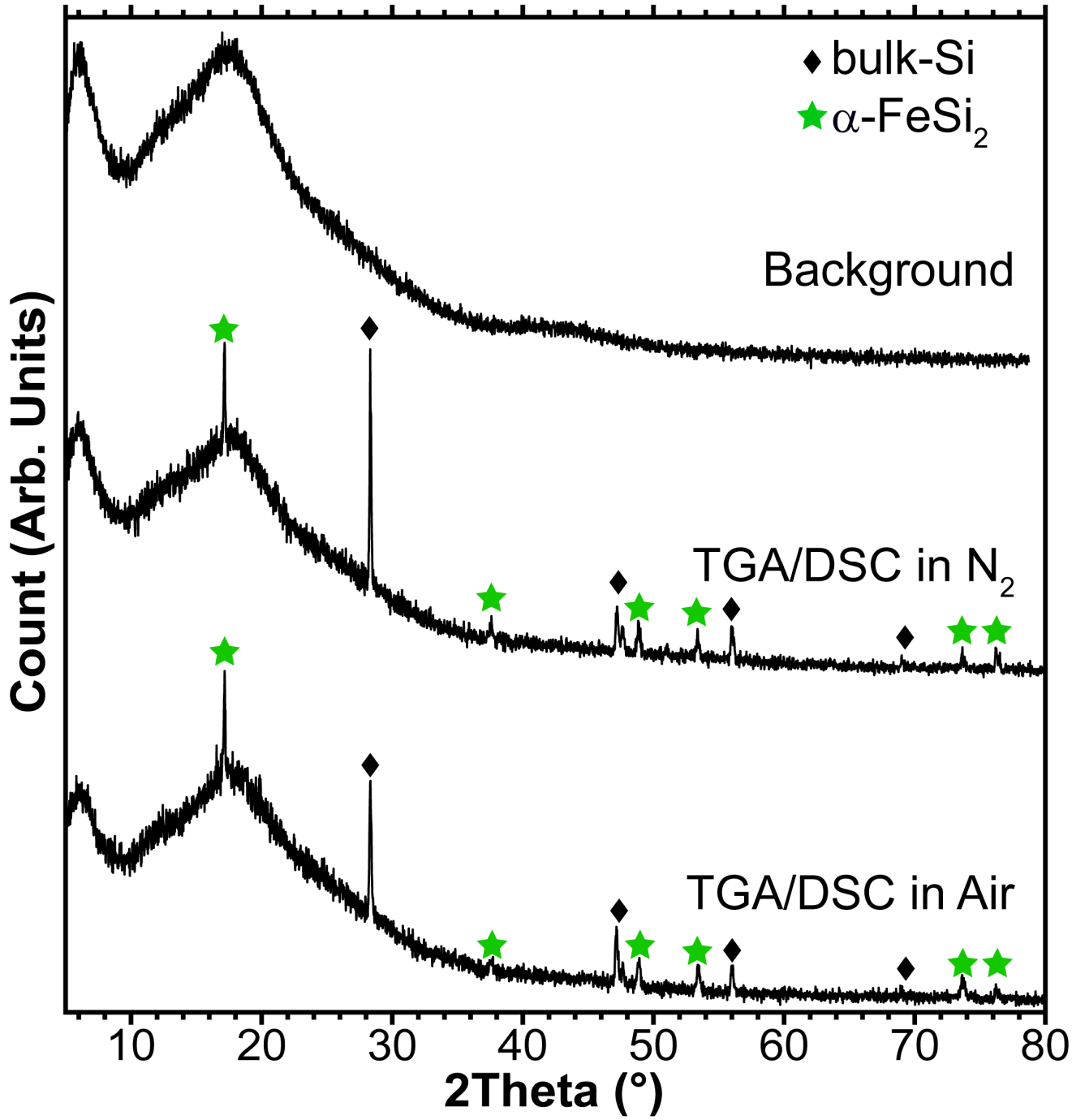

Figure S23. XRD of the product after collecting the TGA/DSC/FTIR/MS data. Green stars correspond to α-$FeSi_2$ and black diamonds correspond to bulk-Si. See Figure S2 for stick pattern and associated PDF number.

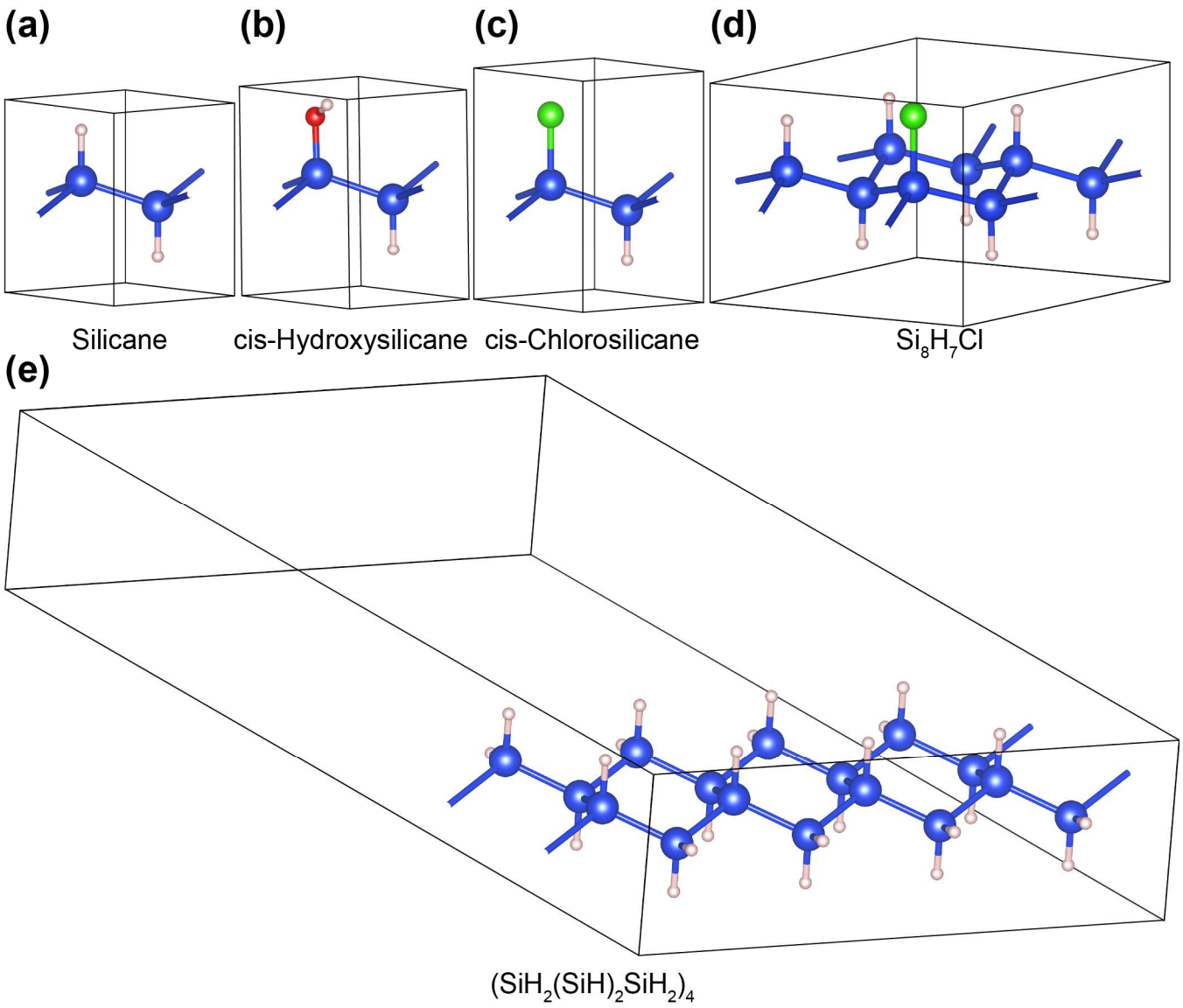

Figure S24. Ball and stick models of the relaxed structures on which DFT calculations of Raman and FTIR were performed. The silicon atoms are blue, hydrogen atoms are white, chlorine atoms are green, and oxygen atoms are red. (a) **Silicane** sheet with 2 silicon atoms and 2 hydrogen atoms per unit cell. (b) Silicane sheet where the top hydrogens have been replaced with hydroxyl groups (i.e., **cis-Hydroxysilicane**). (c) Silicane sheet where the top hydrogens have been replaced with a chlorine atom (i.e., **cis-Chlorosilicane**). (d) Silicane sheet with a chlorine atom attached to a central silicon atom (i.e., **Si_8H_7Cl**). (e) Semi-infinite silicane NS with the two outer rows containing SiH_2 groups and the inner two rows containing SiH groups (i.e., **$(SiH_2(SiH)_2SiH_2)_4$**); vacuum spacing was introduced to electronically isolate the semi-infinite NS. Note that a semi-infinite NS can be thought of as a nanoribbon. These structures have been included in the Supporting Information as a zipped archive.

We also modeled other $Si_{3-n}SiH_nCl$ groups, but the results did not align with experimental data and were therefore omitted. As such, these results indicate that there are very little (if any) Si_2SiHCl or $SiSiH_2Cl$ groups.

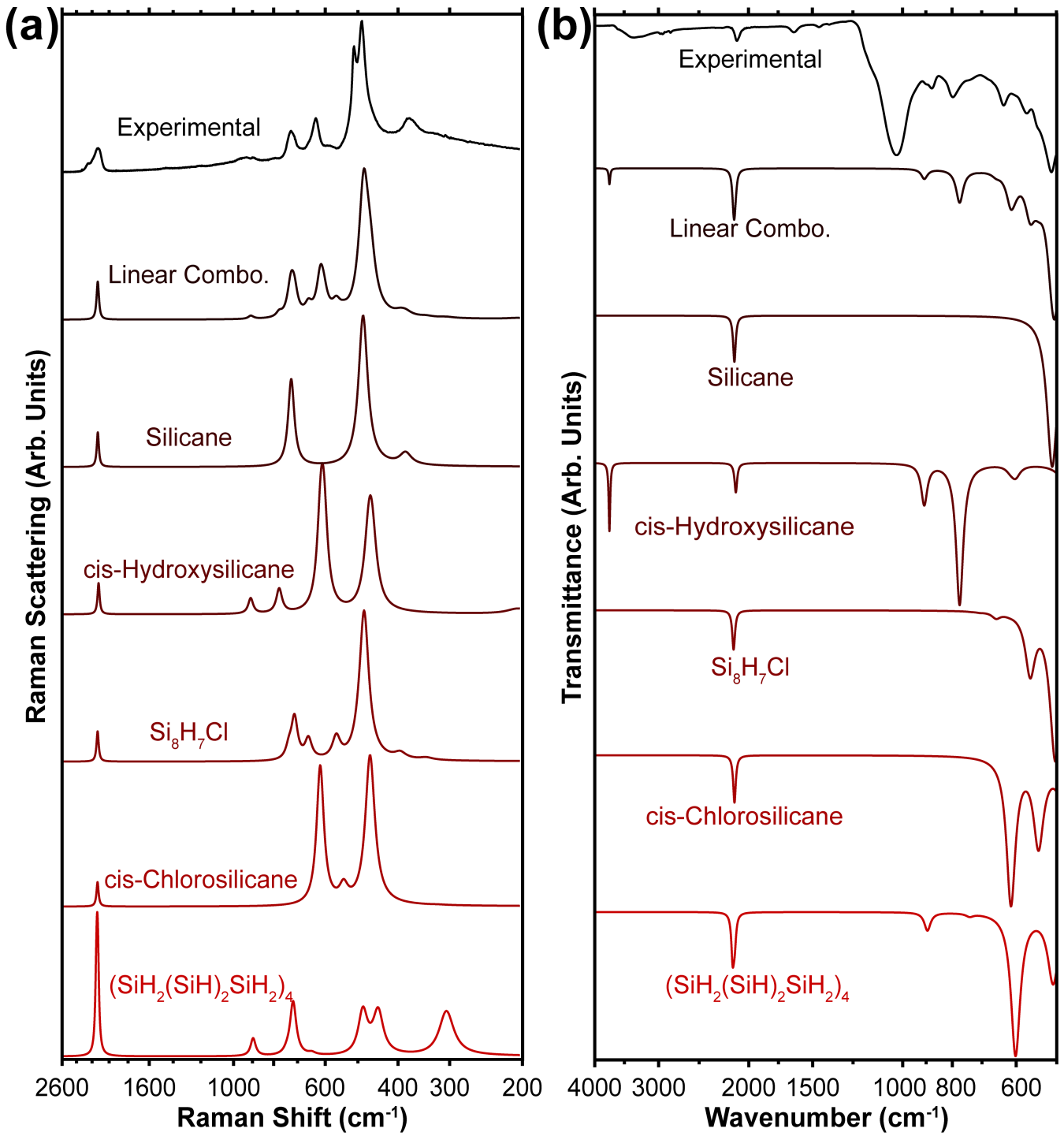

Figure S25. Normalized experimental data and DFT simulations of the vibrational properties of the Si-NSs. The linear combination and the individual components which comprise the linear combination are shown. Panel (a) and (b) correspond to Raman and FTIR, respectively. Experimental data and the linear combination spectra are identical to that which is shown in the main text. Note that the x-axes are plotted on log scale, increasing the apparent width of all peaks in the fingerprint region while compressing the width of all peaks at high wavenumber.

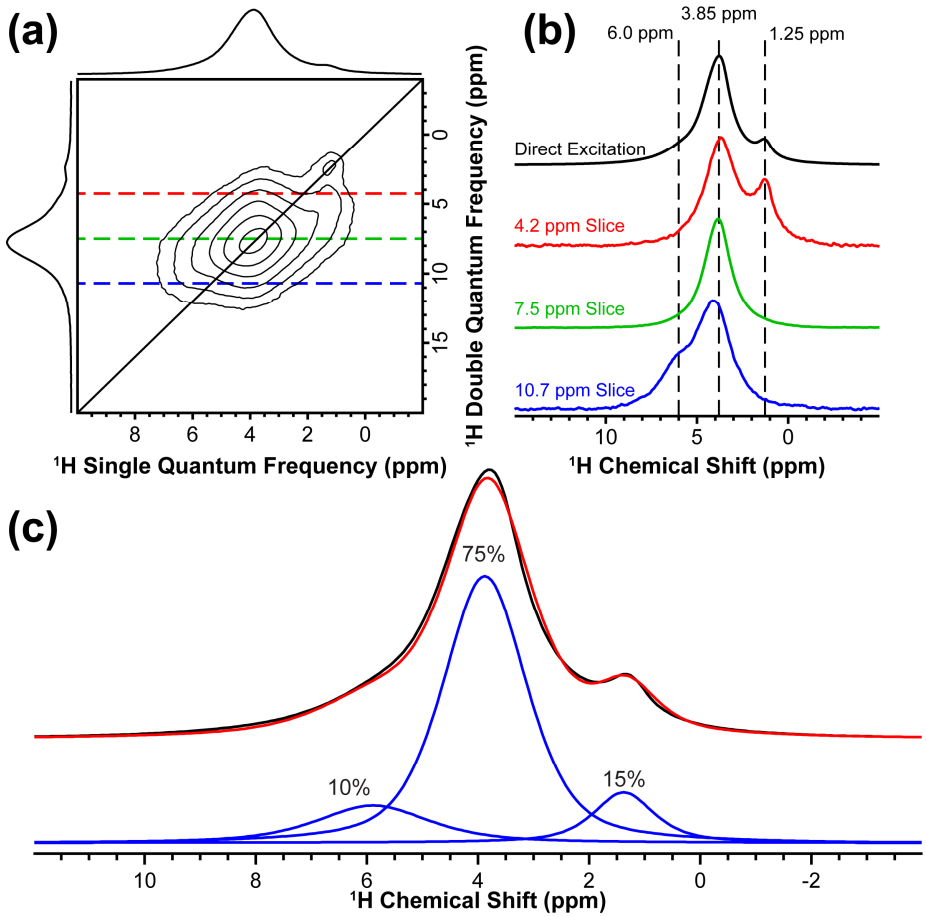

Figure S26. ^{1}H NMR spectra of the Si-NSs. (a) ^{1}H-^{1}H dipolar DQ-SQ homonuclear correlation spectrum; diagonal line indicates autocorrelations and the off-diagonal signals indicate species that are proximate to one another and have a DQ frequency at the sum of the chemical shifts. (b) ^{1}H NMR spectra extracted from selected DQ frequencies from the 2D spectrum in panel (a). (c) ^{1}H peak deconvolution of direct excitation spectrum shown in panel (b); the experimental ^{1}H direct excitation NMR spectrum is shown in black, a three peak fit is shown in red, and the individual peaks which comprise the three peak fit are shown in blue.

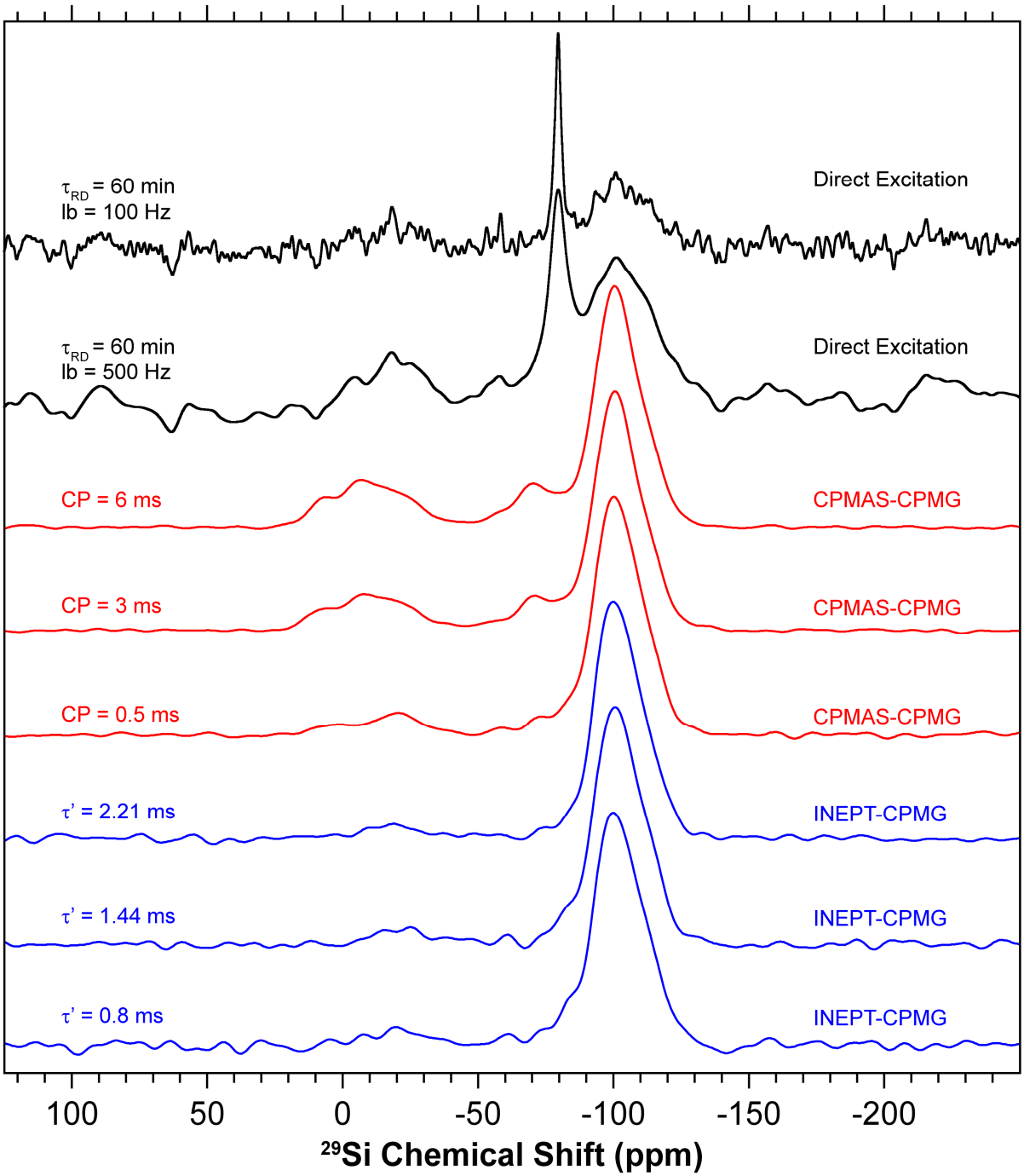

Figure S27. Comparison of ^{29}Si SSNMR spectra obtained with different methods, as indicated on the right of each spectrum. For CPMAS experiments, the spectra were obtained with variable contact times as shown on the left. INEPT spectra were obtained with different INEPT scalar coupling evolution times and are also shown on the left. Both direct excitation spectra were obtained from the same experiment but were processed with different amounts of line broadening to highlight different ^{29}Si NMR signals; this was done because the ^{29}Si signal that arises from the bulk-Si impurity has a much smaller full width at half maximum (FWHM). When a large amount of line broadening is applied, this distorts the intensity of the peaks relative to the other ^{29}Si NMR signals.

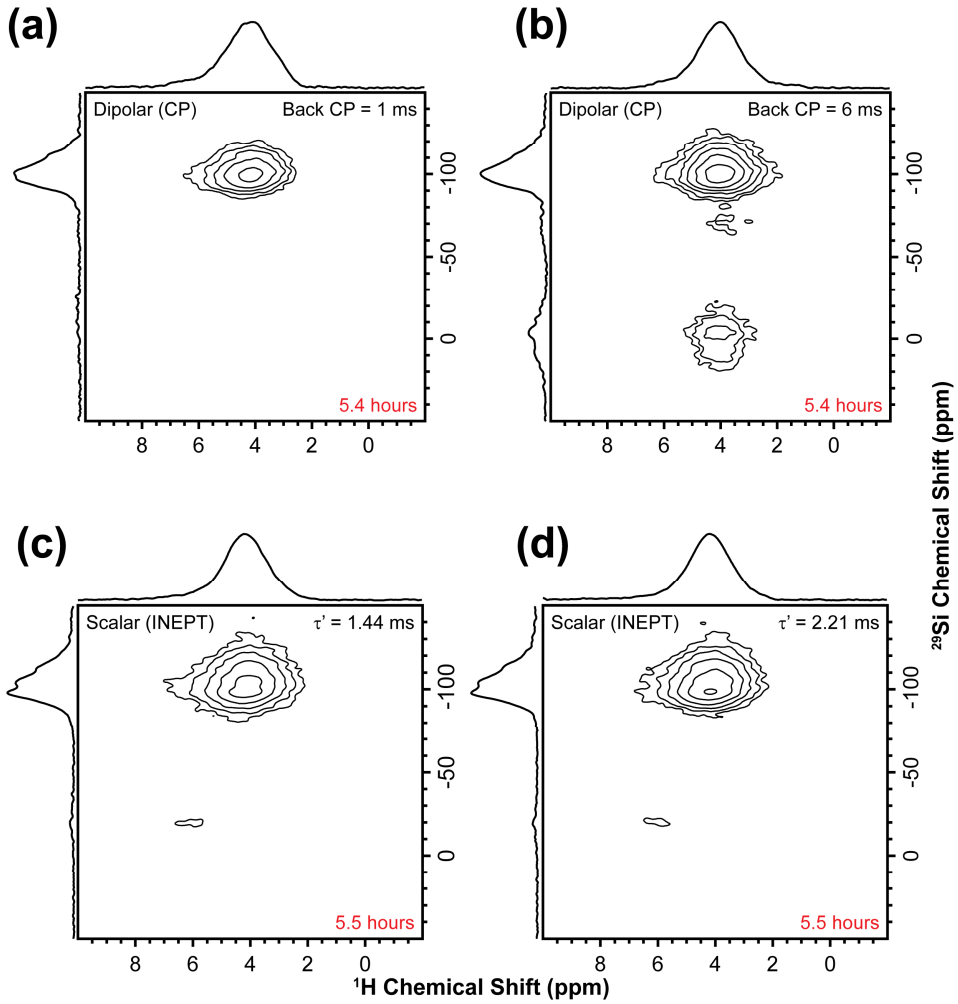

Figure S28. Proton detected 2D ^{1}H-^{29}Si HETCOR SSNMR spectra of the Si-NSs. (a, b) 2D dipolar ^{1}H-^{29}Si CP-HETCOR spectra acquired with a CP forward contact time of 6 ms and a CP back contact time of 1 ms (a) and 6 ms (b). (c, d) 2D scalar ^{1}H-^{29}Si CP-refocused INEPT HETCOR spectra acquired with a CP contact time of 6 ms and τ and τ' mixing times of 1.44 ms (c) and 2.21 ms (d). The total experiment times of the HETCOR spectra is noted in the bottom right corners in red text.

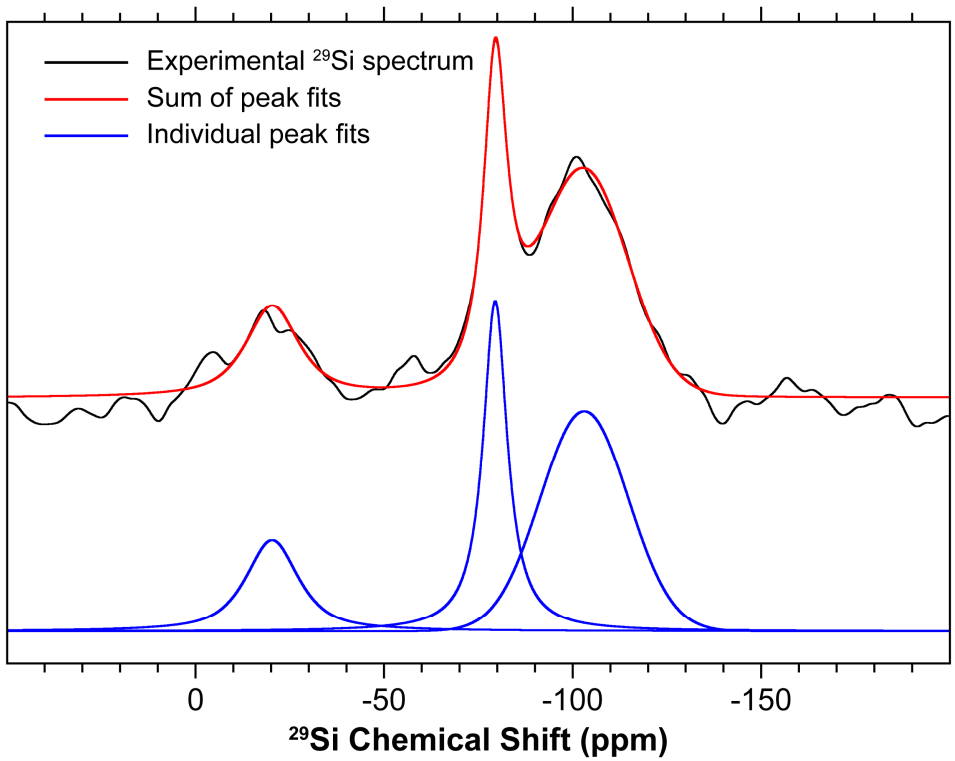

Figure S29. ^{29}Si direct excitation spectrum processed with 500 Hz of line broadening with a three peak fit to estimate the percentage of the bulk-Si impurity. (Top) Experimental ^{29}Si spectrum with an overlay of the sum of the three peak. (Lower) Individual peak fits of the experimental spectrum. From the integral of the three peak fit, we estimate that ~30% of the signal comes from bulk-Si impurities.

Table S7. **^{29}**Si direct excitation peak fitting parameters for the three peak fit shown in Figure S29.

Site	δ_{iso} (ppm)	Linewidth (Hz)	xG/(1–x)L[a]	Integral Area (%)
1	–22.3	1322	0.25	17
2	–81.4	609	0.00	32
3	–105.1	2177	1.00	51

[a] Fitting parameter from the SOLA software for determining the Gaussian or Lorentzian characteristic of the peak.

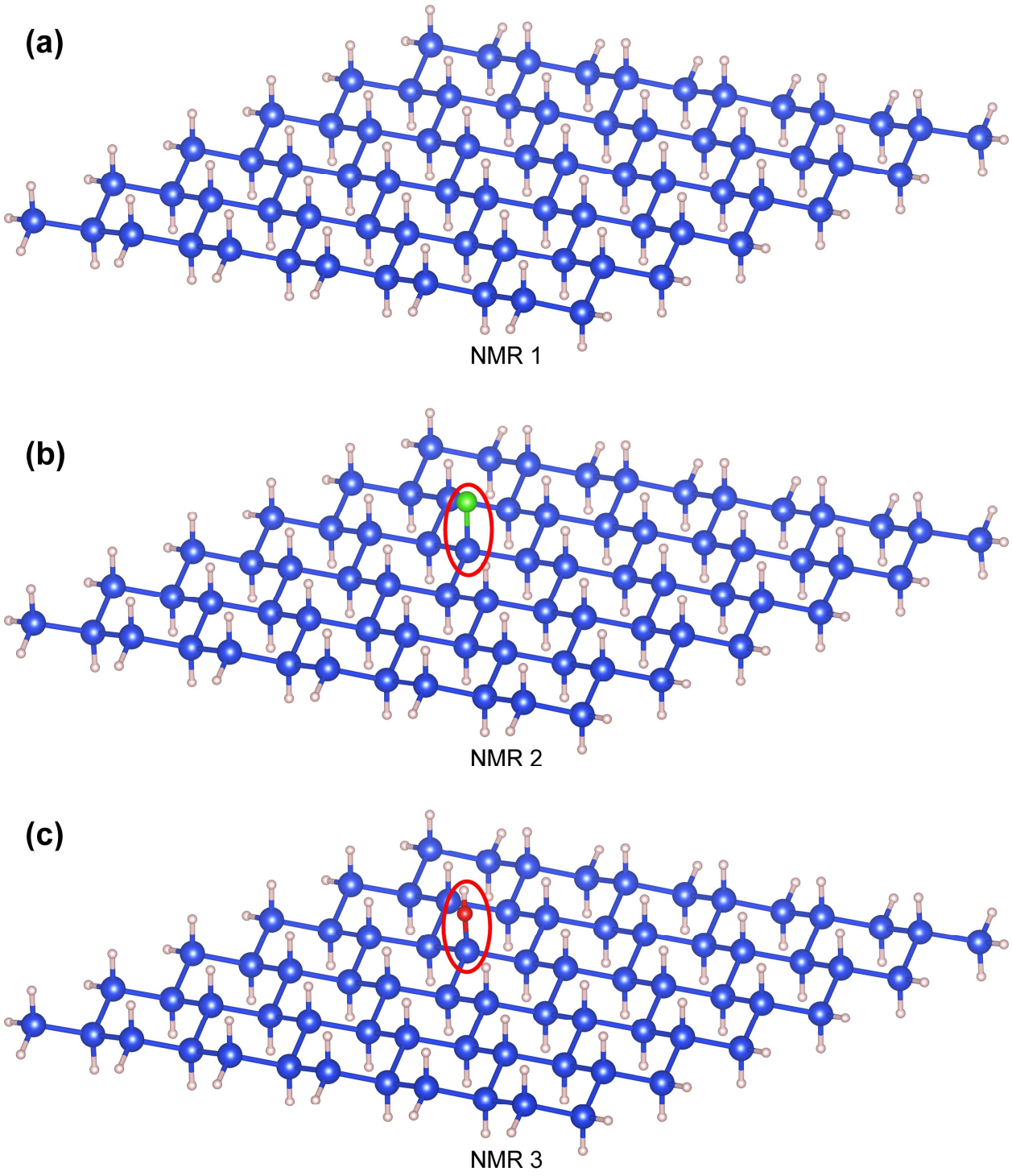

Figure S30. Ball and stick models of the relaxed structures of the three finite sheet models on which the periodic planewave DFT SSNMR calculations were performed. (a) **NMR 1**, all silicon atoms terminated with hydrogen. (b) **NMR 2**, a single silicon atom in the center of the sheet is terminated with a chlorine atom. (c) **NMR 3**, a single silicon atom in the center of the sheet is terminated with a hydroxyl group. The silicon atoms are blue, hydrogen atoms are white, chlorine atoms are green, and oxygen atoms are red. For (b) and (c), the central silicon atom terminated with either a chlorine or hydroxyl group is circled in red. These structures have been included in the Supporting Information as a zipped archive.

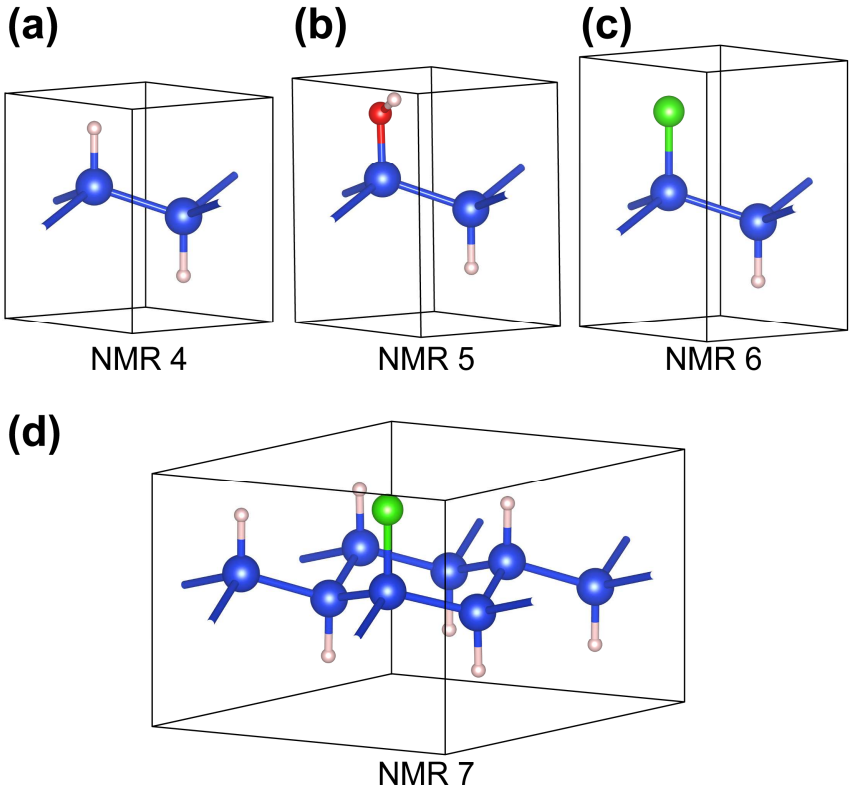

Figure S31. Ball and stick models of the relaxed structures of the four infinite sheet models on which the periodic planewave DFT SSNMR calculations were performed. (a) **NMR 4**, a silicane sheet with 2 silicon atoms and 2 hydrogen atoms. (b) **NMR 5**, a silicane sheet where one of the hydrogens has been replaced with a hydroxyl group (i.e., cis-hydroxysilicane). (c) **NMR 6**, a silicane sheet where one of the hydrogens has been replaced with a chlorine atom (i.e., cis-chlorosilicane). (d) **NMR 7**, a silicane sheet with a chlorine atom attached to a central silicon atom (i.e., **Si_8H_7Cl**). The silicon atoms are blue, hydrogen atoms are white, chlorine atoms are green, and oxygen atoms are red. These structures have been included in the Supporting Information as a zipped archive.

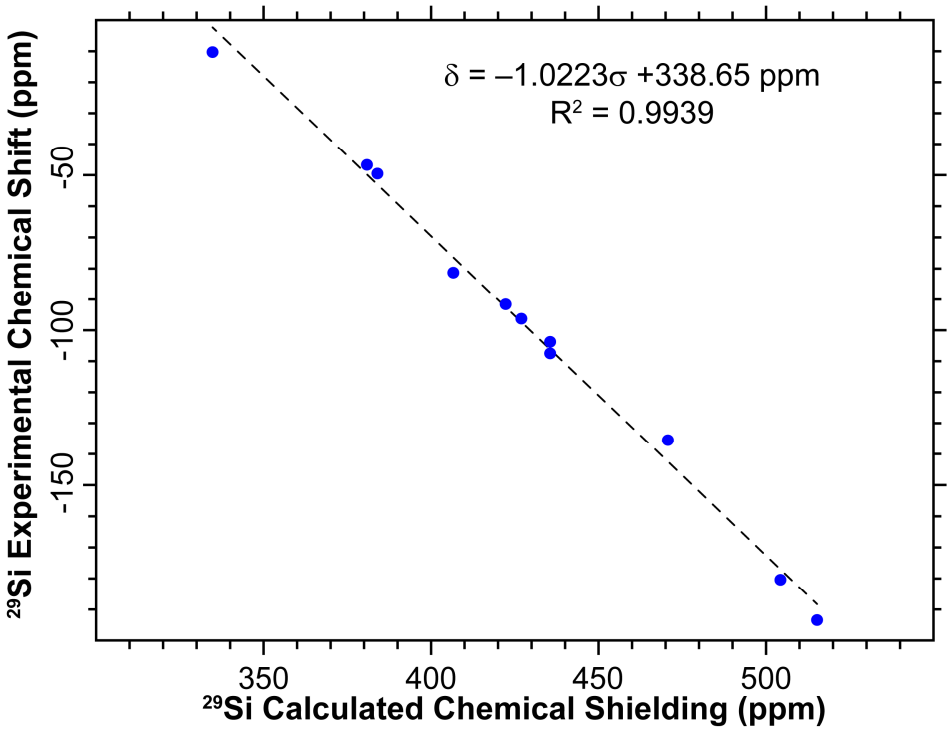

Figure S32. ^{29}Si NMR chemical shielding to chemical shift calibration curve. The compounds used for the chemical shifts calculated shielding and experimental shift values can be found in Table S8.

Table S8. Calculated ^{29}Si chemical shielding and experimental chemical shifts of silicon compounds used to create the calibration plot in Figure S32.

Compound	Calculated Chemical Shielding (ppm)	Experimental Chemical Shift (ppm)	Reference
Bulk-Si (Si)	387.61	–81	58, 59
α-Quartz (SiO_2)	435.5	–107.5	**39**
Tetrakis(trimethylsilyl)silane	334.16 470.53	–9.8 –135.4	**40**
Albite ($NaAlSi_3O_8$)	422.01 426.58 435.42	–91.8 –96.1 –103.9	**41**
$MgSiO_3$ (Perovskite)	515.73	–193	**42**
$MgSiO_3$ (Akimotoite)	504.4	–180.3	**42**
α-Si_3N_4	380.64 383.54	–46.9 –49	**39**

Table S9. Summary of the ^{29}Si and ^{1}H chemical shifts calculated for the structures **NMR 1-7**. The following equations were used to convert the calculated chemical shielding values to calculated chemical shifts for ^{1}H ($\boldsymbol{\delta = -0.923\sigma + 27.5\ ppm}$),[43] and ^{29}Si ($\boldsymbol{\delta = -1.0223\sigma + 338.65\ ppm}$).

Species	Average ^{29}Si Chemical Shift (ppm)	Range of ^{29}Si Chemical Shifts (ppm)	Average ^{1}H Chemical Shift (ppm)	Range of ^{1}H Chemical Shifts (ppm)
NMR 1				
*SiH	–98.92	–112.72 - –93.86	3.36	2.52 - 3.81
*SiH_2	–100.08	–102.45 - –98.91	2.75	2.62 - 2.83
*SiH_3	–101.16	–101.22 - –101.11	2.44	2.33 - 2.50
NMR 2				
*SiH	–98.39	–114.43 - –84.66	3.26	2.49 - 4.06
*SiH_2	–99.48	–102.02 - –98.21	2.72	2.57 - 2.82
*SiH_3	–100.90	–100.91 - –100.90	2.43	2.30 - 2.50
*SiCl	15.25	15.25	-	-
NMR 3				
*SiH	–98.92	–113.12 - –92.54	3.30	2.52 – 3.91
*SiH_2	–99.81	–102.14 - –98.24	2.74	2.60 – 2.83
*SiH_3	–101.14	–101.14 - –101.13	2.43	2.31 – 2.50
*SiOH	23.43	23.43	0.13	0.13
NMR 4				
*SiH	–99.99	–99.99	3.68	3.68
NMR 5				
*SiH	–102.61	–102.61	3.55	3.55
*SiOH	31.63	31.63	0.47	0.47
NMR 6				
*SiH	–93.38	–93.38	3.84	3.84
*SiCl	17.12	17.12	-	-
NMR 7				
*SiH	–87.00	–92.91 - –79.49	1.33	1.13 - 1.46
*SiCl	23.56	23.56	-	-

The SSNMR DFT calculation of ^{1}H and ^{29}Si chemical shifts are in good agreement with experimental chemical shifts.

* Indicates any arbitrary chemical attachment.

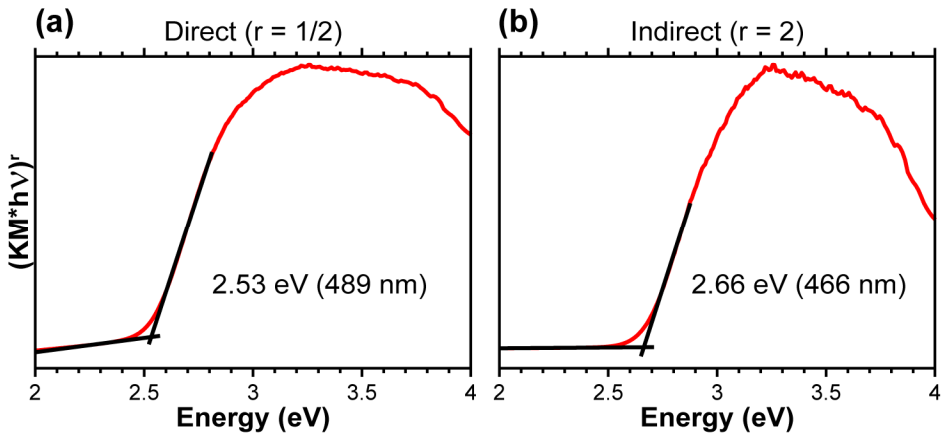

Figure S33. Tauc plots of the Kubelka-Munk transformation of diffuse reflectance data fitted to (a) direct and (b) indirect band gaps.

Table S10. Peak fitting parameters corresponding to the curves shown in steady state photoluminescence in Figure 4b of the main text. Parameters were determined with a GLP distribution by minimizing the sum of squared residuals. The GLP formula is shown in Equation S1.

Center (nm)	Area (%)	FWHM	I	m
498.0	64	0.31	0.80	62.02
543.9	36	0.48	0.31	22.00

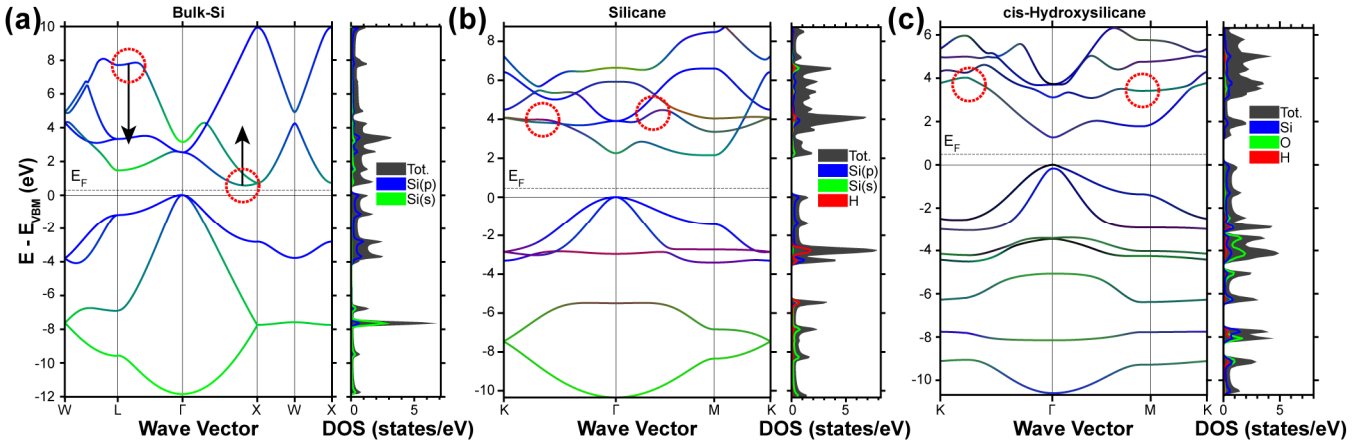

Figure S34. Band structure of (a) bulk-Si, (b) Silicane, and (c) cis-Hydroxysilicane. Dashed red circles represent locations before and after confinement and forming SiH or SiOH bonds. Note that only a finite number of bands were calculated, so the DOS at high energies is not necessarily complete.

It is hypothesized that the circled areas in Figure S34a move towards what is shown in Figure S34b and Figure S34c, pulling the bulk-Si ~7.5 eV band between L and Γ downwards in energy while the band associated with the indirect transition of bulk-Si near X is pushed up in energy.

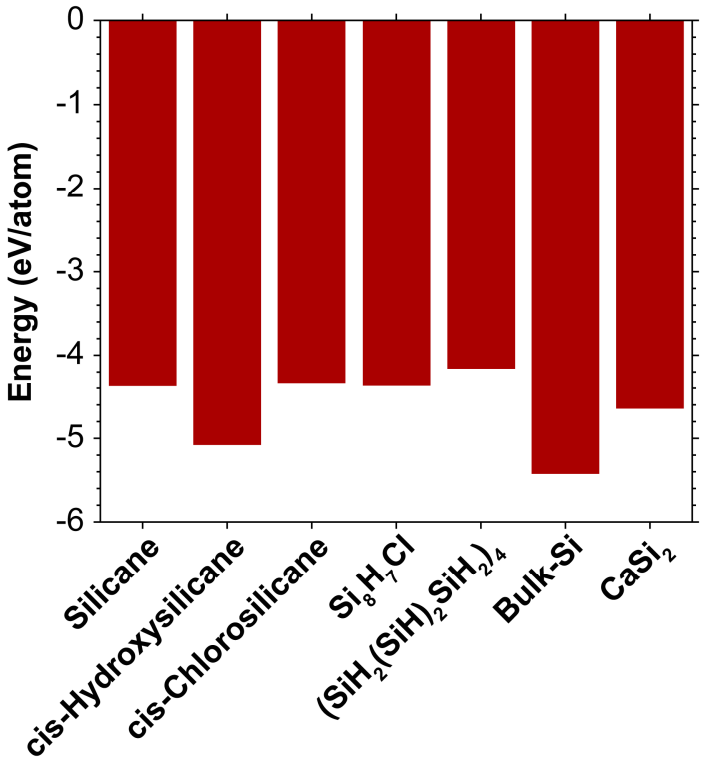

Figure S35. Converged energies of the relaxed structures from which FTIR and Raman vibrational modes were calculated. See Figure S24 for ball and stick model. The more negative the energy, the more thermodynamically stable the structure.

References:

(1) Cory, D. G.; Ritchey, W. M. Suppression of Signals from the Probe in Bloch Decay Spectra. *J. Magn. Reson. 1969* **1988**, *80* (1), 128–132.

(2) Feike, M.; Demco, D. E.; Graf, R.; Gottwald, J.; Hafner, S.; Spiess, H. W. Broadband Multiple-Quantum NMR Spectroscopy. *J. Magn. Reson. A* **1996**, *122* (2), 214–221.

(3) Schnell, I.; Lupulescu, A.; Hafner, S.; Demco, D. E.; Spiess, H. W. Resolution Enhancement in Multiple-Quantum MAS NMR Spectroscopy. *J. Magn. Reson.* **1998**, *133* (1), 61–69.

(4) Schnell, I. Dipolar Recoupling in Fast-MAS Solid-State NMR Spectroscopy. *Prog. Nucl. Magn. Reson. Spectrosc.* **2004**, *45* (1), 145–207.

(5) Ishii, Y.; Tycko, R. Sensitivity Enhancement in Solid State 15N NMR by Indirect Detection with High-Speed Magic Angle Spinning. *J. Magn. Reson.* **2000**, *142* (1), 199–204.

(6) Ishii, Y.; Yesinowski, J. P.; Tycko, R. Sensitivity Enhancement in Solid-State ^{13}C NMR of Synthetic Polymers and Biopolymers by ^{1}H NMR Detection with High-Speed Magic Angle Spinning. *J. Am. Chem. Soc.* **2001**, *123* (12), 2921–2922.

(7) Wiench, J. W.; Bronnimann, C. E.; Lin, V. S.-Y.; Pruski, M. Chemical Shift Correlation NMR Spectroscopy with Indirect Detection in Fast Rotating Solids: Studies of Organically Functionalized Mesoporous Silicas. *J. Am. Chem. Soc.* **2007**, *129* (40), 12076–12077.

(8) Mao, K.; Wiench, J. W.; Lin, V. S.-Y.; Pruski, M. Indirectly Detected Through-Bond Chemical Shift Correlation NMR Spectroscopy in Solids under Fast MAS: Studies of Organic–Inorganic Hybrid Materials. *J. Magn. Reson.* **2009**, *196* (1), 92–95.

(9) Mao, K.; Pruski, M. Directly and Indirectly Detected Through-Bond Heteronuclear Correlation Solid-State NMR Spectroscopy under Fast MAS. *J. Magn. Reson.* **2009**, *201* (2), 165–174.

(10) Elena, B.; Lesage, A.; Steuernagel, S.; Böckmann, A.; Emsley, L. Proton to Carbon-13 INEPT in Solid-State NMR Spectroscopy. *J. Am. Chem. Soc.* **2005**, *127* (49), 17296–17302.

(11) Hanrahan, M. P.; Fought, E. L.; Windus, T. L.; Wheeler, L. M.; Anderson, N. C.; Neale, N. R.; Rossini, A. J. Characterization of Silicon Nanocrystal Surfaces by Multidimensional Solid-State NMR Spectroscopy. *Chem. Mater.* **2017**, *29* (24), 10339–10351.

(12) Trébosc, J.; Wiench, J. W.; Huh, S.; Lin, V. S.-Y.; Pruski, M. Solid-State NMR Study of MCM-41-Type Mesoporous Silica Nanoparticles. *J. Am. Chem. Soc.* **2005**, *127* (9), 3057–3068.

(13) Lesage, A.; Auger, C.; Caldarelli, S.; Emsley, L. Determination of Through-Bond Carbon−Carbon Connectivities in Solid-State NMR Using the INADEQUATE Experiment. *J. Am. Chem. Soc.* **1997**, *119* (33), 7867–7868.

(14) Sakellariou, D.; Lesage, A.; Hodgkinson, P.; Emsley, L. Homonuclear Dipolar Decoupling in Solid-State NMR Using Continuous Phase Modulation. *Chem. Phys. Lett.* **2000**, *319* (3), 253–260.

(15) Brandt, M. S.; Fuchs, H. D.; Stutzmann, M.; Weber, J.; Cardona, M. The Origin of Visible Luminescencefrom "Porous Silicon": A New Interpretation. *Solid State Commun.* **1992**, *81* (4), 307–312.

(16) Molassioti-dohms, A.; Dettlaff-weglikowska, U.; Finkbeiner, S.; Hönle, W.; Weber, J. Photo- and Chemiluminescence from Wöhler Siloxenes. *J. Electrochem. Soc.* **1996**, *143* (8), 2674-2677

(17) Weiss, A.; Beil, G.; Meyer, H. The Topochemical Reaction of $CaSi_2$ to a Two-Dimensional Subsiliceous Acid $Si_6H_3(OH)_3$ (= Kautskys' Siloxene). *Z. Für Naturforschung B* **1979**, *35* (1), 25–30.

(18) Deák, P.; Rosenbauer, M.; Stutzmann, M.; Weber, J.; Brandt, M. S. Siloxene: Chemical Quantum Confinement Due to Oxygen in a Silicon Matrix. *Phys. Rev. Lett.* **1992**, *69* (17), 2531–2534.

(19) Fuchs, H. D.; Stutzmann, M.; Brandt, M. S.; Rosenbauer, M.; Weber, J.; Cardona, M. Visible Luminescence from Porous Silicon and Siloxene. *Phys. Scr.* **1992**, *1992* (T45), 309.

(20) Meng, X.; Sasaki, K.; Sano, K.; Yuan, P.; Tatsuoka, H. Synthesis of Crystalline Si-Based Nanosheets by Extraction of Ca from CaSi2 in Inositol Hexakisphosphate Solution. *Jpn. J. Appl. Phys.* **2017**, *56* (5S1), 05DE02.

(21) Fuchs, H. D.; Stutzmann, M.; Brandt, M. S.; Rosenbauer, M.; Weber, J.; Breitschwerdt, A.; Deák, P.; Cardona, M. Porous Silicon and Siloxene: Vibrational and Structural Properties. *Phys. Rev. B* **1993**, *48* (11), 8172–8189.

(22) Hessel, C. M.; Wei, J.; Reid, D.; Fujii, H.; Downer, M. C.; Korgel, B. A. Raman Spectroscopy of Oxide-Embedded and Ligand-Stabilized Silicon Nanocrystals. *J. Phys. Chem. Lett.* **2012**, *3* (9), 1089–1093.

(23) Uchinokura, K.; Sekine, T.; Matsuura, E. Raman Scattering by Silicon. *Solid State Commun.* **1972**, *11* (1), 47–49.

(24) Parker, J. H.; Feldman, D. W.; Ashkin, M. Raman Scattering by Silicon and Germanium. *Phys. Rev.* **1967**, *155* (3), 712–714.

(25) Quiroga-González, E.; Carstensen, J.; Glynn, C.; O'Dwyer, C.; Föll, H. Pore Size Modulation in Electrochemically Etched Macroporous P-Type Silicon Monitored by FFT Impedance Spectroscopy and Raman Scattering. *Phys. Chem. Chem. Phys.* **2013**, *16* (1), 255–263.

(26) Brodsky, M. H.; Cardona, M.; Cuomo, J. J. Infrared and Raman Spectra of the Silicon-Hydrogen Bonds in Amorphous Silicon Prepared by Glow Discharge and Sputtering. *Phys. Rev. B* **1977**, *16* (8), 3556–3571.

(27) Durig, J. R.; Sullivan, J. F.; Qtaitat, M. A. Infrared and Raman Spectra, Conformational Stability, Barriers to Internal Rotation, Ab Initio Calculations, Ro Structure, and Vibrational Assignment for Methyl Vinyl Silane. *J. Mol. Struct.* **1991**, *243* (3), 239–273.

(28) Cardona, M. Vibrations in Amorphous Silicon and Its Alloys. *J. Mol. Struct.* **1986**, *141*, 93–107.

(29) Johnson, E. V.; Kroely, L.; Roca i Cabarrocas, P. Raman Scattering Analysis of SiH Bond Stretching Modes in Hydrogenated Microcrystalline Silicon for Use in Thin-Film Photovoltaics. *Sol. Energy Mater. Sol. Cells* **2009**, *93* (10), 1904–1906.

(30) Zamanzadeh-Hanebuth, N.; Brandt, M. S.; Stutzmann, M. Vibrational Properties of Siloxene: Isotope Substitution Studies. *J. Non-Cryst. Solids* **1998**, *227–230*, 503–506.
(31) Islam, M. A.; Purkait, T. K.; Veinot, J. G. C. Chloride Surface Terminated Silicon Nanocrystal Mediated Synthesis of Poly(3-Hexylthiophene). *J. Am. Chem. Soc.* **2014**, *136* (43), 15130–15133.
(32) Kalem, S.; Chevallier, J.; Al Dallal, S.; Bourneix, J. Infrared Vibrational Spectra of Chlorinated and Hydrogenated Amorphous Silicon. *J. Phys. Colloq.* **1981**, *42* (C4), C4-361-C4-363.
(33) Yamanaka, S.; Matsu-ura, H.; Ishikawa, M. New Deintercalation Reaction of Calcium from Calcium Disilicide. Synthesis of Layered Polysilane. *Mater. Res. Bull.* **1996**, *31* (3), 307–316.
(34) Griffith, G. W. Quantitation of Silanol in Silicones by FTIR Spectroscopy. *Ind. Eng. Chem. Prod. Res. Dev.* **1984**, *23* (4), 590–593.
(35) Castillo, S. M.; Tang, Z.; Litvinchuk, A. P.; Guloy, A. M. Lattice Dynamics of the Rhombohedral Polymorphs of $CaSi_2$. *Inorg. Chem.* **2016**, *55* (20), 10203–10207.
(36) Karar, D.; Bandyopadhyay, N. R.; Pramanick, A. K.; Acharyya, D.; Conibeer, G.; Banerjee, N.; Kusmartseva, O. E.; Ray, M. Quasi-Two-Dimensional Luminescent Silicon Nanosheets. *J. Phys. Chem. C.* **2018**. *122* (33) 18912-18921.
(37) Holzman, G. R.; Lauterbur, P. C.; Anderson, J. H.; Koth, W. Nuclear Magnetic Resonance Field Shifts of Si29 in Various Materials. *J. Chem. Phys.* **1956**, *25* (1), 172–173.
(38) Giuliani, J. R.; Harley, S. J.; Carter, R. S.; Power, P. P.; Augustine, M. P. Using Liquid and Solid State NMR and Photoluminescence to Study the Synthesis and Solubility Properties of Amine Capped Silicon Nanoparticles. *Solid State Nucl. Magn. Reson.* **2007**, *32* (1), 1–10.
(39) Chollon, G.; Hany, R.; Vogt, U.; Berroth, K. A Silicon-29 MAS–NMR Study of α-Silicon Nitride and Amorphous Silicon Oxynitride Fibres. *J. Eur. Ceram. Soc.* **1998**, *18* (5), 535–541.
(40) Hayashi, S.; Hayamizu, K. Chemical Shift Standards in High-Resolution Solid-State NMR (1) ^{13}C, ^{29}Si, and ^{1}H Nuclei. *Bull. Chem. Soc. Jpn.* **1991**, *64* (2), 685–687.
(41) Shore, J. S.; DePaul, S. M.; Ernst, M.; Phillips, B. L. Double-Resonance and Two-Dimensional Silicon-29 NMR Spectroscopy of Minerals. In *Solid-State NMR Spectroscopy of Inorganic Materials*; ACS Symposium Series; American Chemical Society, **1999**, *717*, 305–325.
(42) Ashbrook, S. E.; Berry, A. J.; Frost, D. J.; Gregorovic, A.; Pickard, C. J.; Readman, J. E.; Wimperis, S. ^{17}O and ^{29}Si NMR Parameters of $MgSiO_3$ Phases from High-Resolution Solid-State NMR Spectroscopy and First-Principles Calculations. *J. Am. Chem. Soc.* **2007**, *129* (43), 13213–13224.
(43) Carnahan, S. L.; Lampkin, B. J.; Naik, P.; Hanrahan, M. P.; Slowing, I. I.; VanVeller, B.; Wu, G.; Rossini, A. J. Probing O–H Bonding through Proton Detected ^{1}H–^{17}O Double Resonance Solid-State NMR Spectroscopy. *J. Am. Chem. Soc.* **2019**, *141* (1), 441–450.